Distance Dependence of Electronic Coupling in Rigid, Cofacially Compressed, π-Stacked Organic Mixed-Valence Systems

Hae Won Jung,[†] Sung Ewn Yoon,[†] Patrick J. Carroll,[‡] Michael R. Gau,[‡] Michael J. Therien[§]* and Youn K. Kang.[†]*

[†]Department of Chemistry, Sangmyung University, Seoul, 03016, Korea

[‡]Department of Chemistry, University of Pennsylvania, Philadelphia, Pennsylvania, 19104

[§|]Department of Chemistry, Duke University, Durham, North Carolina, 27708.

* Corresponding Authors

Michael J. Therien michael.therien@duke.edu

Youn K. Kang younkang@smu.ac.kr

ABSTRACT. A series of new π-stacked compounds, 1,8-bis(2',5'-dimethoxybenzene-1'-yl)naphthalene (**1**), 1,4-bis(8'-(2",5"-dimethoxybenzene-1"-yl)naphthalen-1'-yl)benzene (**2**), and 1,8-bis(4'-(8"-(2"',5"'-dimethoxybenzene-1"'-yl)naphthalen-1"-yl)benzene-1'-yl)naphthalene (**3**), have been synthesized and characterized herein as precursor molecules of monocationic mixed-valence systems (MVSs). The three-dimensional geometries of these compounds were determined by X-ray crystallography. A near-orthogonal alignment of the naphthalene pillaring motif to the dimethoxybenzene redox center, or the phenylene spacer, imposes cofacial alignment of these units in a juxtaposed manner with sub-van der Waals interplanar distances. The centroid-to-centroid distances of the two dimethoxybenezene rings in these mixed-valence systems are estimated to be 3.24, 7.08, and 10.35 Å for $\mathbf{1}^{\bullet+}$, $\mathbf{2}^{\bullet+}$, and $\mathbf{3}^{\bullet+}$, respectively, by crystallography-based density functional theory (DFT) calculations. Cyclic and differential pulse voltammograms reveal that the ΔE values between two sequential oxidation potentials are 0.30, 0.11, and 0.10 V for **1**, **2**, and **3**, respectively. MVSs derived from these compounds are recognized as class II according to Robin and Day classification. The decay parameter β, that describes the distance dependence of the squared electronic coupling in the three mixed valence systems was experimentally determined via Mulliken-Hush analysis of the intervalence charge transfer band (β = 0.37 $Å^{-1}$), and theoretically assessed from charge-resonance contributions derived from DFT computations (β = 0.37 $Å^{-1}$). These values are extraordinarily mild, indicating that the electronic interaction between redox centers in the longitudinal direction may be comparable to that in the transverse direction, if the MVS system is appropriately designed.

Introduction

The use of organic small molecules and conjugated polymers as charge transporting materials is increasingly prominent in modern electronic devices.[1-15] For the improvement of the performance of organic electronic devices, information regarding mutual electronic interactions between the constituent organic building blocks, which includes the longitudinal interaction through π-stacked aromatic units in particular, is crucial. The electronic coupling (H_{12}), the off-diagonal Hamiltonian matrix element in the secular determinant quantifying the degree of mixing of electronic wavefunctions of two diabatic states, is often used to describe the degree of electronic interaction between the geometrically separated two redox centers.[16] Importantly, the distance dependence of electronic coupling has been proven to be one of the most reliable measures of the charge tunneling capability of the medium. The squared electronic coupling is expected to decrease exponentially with distance (eq. 1); the nature of this exponential decay is expressed by the decay parameter (β), which is sensitive to the electronic nature of the redox centers and tunneling medium.[17-21]

$$|H_{12}|^2 = |H_0|^2 \exp[-\beta(R_{12} - R_0)] \qquad \text{(eq.1)}$$

In eq. 1, H_{12} is the electronic coupling at R_{12}, H_0 is the electronic coupling at R_0, R_{12} is the distance of two redox centers, and R_0 is the smallest possible separation distance ($\sim$3.0 Å). Extensive efforts have been devoted to explore how the type of the molecular structures impacts the magnitude of H_{12} values. Exemplary charge tunneling media that have been investigated include various types of conjugated and unconjugated covalent bonds, H-bonds, and biological structural motives such as peptides, proteins, and DNA.[21]

An issue that had been debated was the distance dependence of electronic coupling in π-stacked cofacial aromatic units. Wide ranges of β values (~0.2 - ~1.0) have been reported for double-stranded DNA models.[22-29] Studies that examined unusually rigid, π-stacked cofacial porphyrin donor (**P**)-aromatic spacer-quinone acceptor systems in which these units are held at sub-van der Waals interplanar separations revealed a mild phenomenological distance dependence of electron transfer rate constant (β^k),

with $\beta^k = 0.43$ and 0.35 for photoinduced charge separation (CS) and thermal charge recombination (CR).[21, 30] These values are consistent with those obtained using the generalized Mulliken-Hush analysis approach, in which β = 0.59 and 0.58 was obtained for CS and CR, respectively.[31] Given the limited information regarding the distance dependence of electronic coupling in cofacially compressed organic π-stacked model systems,[32-39] further studies are invaluable to illuminate the design of organic systems having delocalized electronic states.

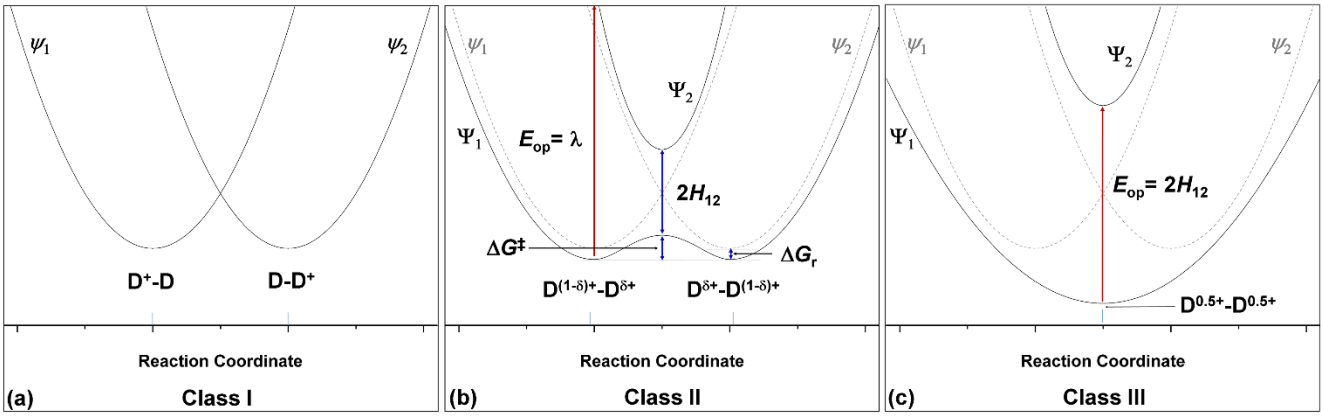

Figure 1. Diabatic (a) and adiabatic free energy surfaces (b, c) of Robin-Day class I (a), II (b), and III (c) mixed valence systems.

Mixed-valence systems (MVSs) are cleverly designed simplified systems in which the reactant (D^+-D, ψ_1) and the product (D-D^+, ψ_2) states of the intramolecular thermal electron transfer reaction are energetically isoergic (ΔG_{ET} = 0) and geometrically symmetric, so that the electronic coupling matrix element between the two states can be easily assessed (Figure 1).[40-57] The energy of the inter-valence charge transfer (IVCT) electronic absorption band corresponds to $2H_{12}$ and the reorganization energy (λ) in Robin-Day class III and class II MVSs, respectively.[40] The H_{12} value of a class II MVS can be accurately evaluated from the experimentally determined transition dipole moment (μ) of the IVCT band[42-43,58-69] using the Mulliken-Hush relation (eq. 2).[16,70-77]

$$H_{12} = 2.06 \times 10^{-2} \frac{\sqrt{\nu_{max} \varepsilon_{max} \Delta \nu_{fwhm}}}{R_{12}} \qquad \text{(eq.2)}$$

Here ν_{max} and $\Delta\nu_{fwhm}$ are the IVCT band maximum frequency and width in wave numbers, ε_{max} is the extinction coefficient at the band maximum in $M^{-1}cm^{-1}$, and R_{12} is the separation distance between two redox centers in Å. The existence of an IVCT band in a MVS represents a straightforward approach to quantify the H_{12} value.

An alternative expression for the evaluation of H_{12}, of similar origins to the Mulliken-Hush relation, is shown below.

$$H_{12} = \Delta E \cdot |C_1 C_2| \qquad \text{(eq.3)}$$

Here, ΔE is the energy gap between two adiabatic states Ψ_1 and Ψ_2 where these two states can be expressed as a linear combination of two diabatic states ψ_1 and ψ_2 as follows.[78]

$$\Psi_1 = C_1\psi_1 + C_2\psi_2 \qquad \text{(eq. 4a)}$$

$$\Psi_2 = C_1\psi_2 - C_2\psi_1 \qquad \text{(eq. 4b)}$$

Since both C_1 and C_2 are normalized ($C_1^2 + C_2^2 = 1$), eq. 3 can be recast as

$$H_{DA} = \left|\Delta E\sqrt{(1-\zeta)\zeta}\right| \qquad \text{(eq. 5)}$$

where $\zeta \approx C_2^2$.[16,79-80]

The ζ value is the degree of ψ_2 character in the Ψ_1 state or that of ψ_1 character in the Ψ_2 state. This value may be spectroscopically determined from the vibrational frequency analysis of transient Raman spectra[81] or visible pump/mid-IR probe transient absorption spectra.[79-80] The determination of the ζ value via bond length analysis of X-ray crystallographic data has also been reported.[82-83]

In this manuscript, we report the distance dependence of electronic coupling in newly synthesized MVSs [1,8-bis(2',5'-dimethoxybenzene-1'-yl)naphthalene]$^{\bullet+}$ (**1**$^{\bullet+}$), [1,4-bis(8'-(2",5"-dimethoxybenzene-1"-yl)naphthalen-1'-yl)benzene]$^{\bullet+}$ (**2**$^{\bullet+}$), and [1,8-bis(4'-(8"-(2"',5"'-dimethoxybenzene-1"'-yl)naphthalen-1"-yl)benzene-1'-yl)naphthalene]$^{\bullet+}$ (**3**$^{\bullet+}$), in which two dimethoxybenzene redox centers, hereinafter designated as **D** (or **D$_1$** and **D$_2$** if necessary), are separated in the rigid, cofacially compressed, π-stacked aromatic framework (Chart 1). Note that ultrafast photoinduced CS and thermal CR reactions through related π-stacked aromatic spacers have been

investigated in the corresponding porphyrin-spacer-quinone archetype;[30,84] these studies exclude the possibility of charge transfer through the orthogonally attached naphthalene pillars, and underscore that donor-acceptor electronic coupling is mediated through the π-stacked aromatic units. Experimental and computational data acquired for MVSs $\mathbf{1}^{\bullet+}$-$\mathbf{3}^{\bullet+}$ show that the distance dependence of electronic coupling is surprisingly mild relative to that determined from photo-induced charge separation and thermal charge recombination data acquired from pump-probe transient absorption spectroscopy.[21]

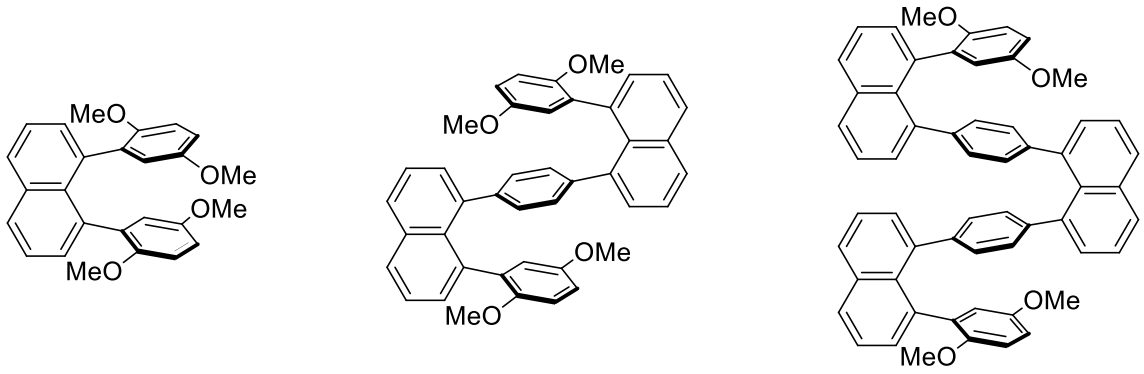

1 **2** **3**

Chart 1. Structures of 1,8-bis(2',5'-dimethoxybenzene-1'-yl)naphthalene (**1**), 1,4-bis(8'-(2",5"-dimethoxybenzene-1"-yl)naphthalen-1'-yl)benzene (**2**), 1,8-bis(4'-(8"-(2"',5"'-dimethoxybenzene-1"'-yl)naphthalen-1"-yl)benzene-1'-yl)naphthalene (**3**).

Experimental Section

1. Synthesis and Characterizations. A full account of the synthesis and characterization data for all new compounds, complete with detailed reaction schemes and NMR spectra, is provided in the Supporting Information.

2. Instrumentation. NMR spectra were recorded on a 500-MHz Avance III Bruker spectrometer. Chemical shifts for ^{1}H NMR and ^{13}C NMR spectra are relative to residual protium in the deuterated solvents ($CDCl_3$, $\delta = 7.24$ for ^{1}H NMR and $\delta = 77$ for ^{13}C NMR). All coupling constants are reported in Hertz. High-resolution mass spectrometry (HRMS) data were obtained at the Korea Basic Science Institute (Daegu). Cyclic voltammograms and differential pulse voltammograms were obtained using an IVIUM Compactstat. Glassy carbon and Ag/Ag^{+} (0.01 M $AgNO_3$) were used as working and reference

electrodes, respectively. A platinum wire was used as the counter electrode. The ferrocene/ferrocenium redox couple was used as an internal reference. The scan rate was maintained at 180 mV/s. Cyclic and differential pulse voltammetric measurements were performed under nitrogen atmosphere using an electrochemical solution containing 4 mM of the synthesized compounds and 0.1 M tetrabutylammonium hexafluorophosphate ($TBAPF_6$) in a spectroscopic grade solvent mixture (CH_2Cl_2:CH_3CN = 3:2 v/v), which had been purged with dry nitrogen gas for 10 min. Electronic spectra were recorded on an Agilent UV/vis/NIR spectrophotometry system. Spectroelectrochemical measurements were carried out in an optically transparent thin-layer electrochemical (OTTLE) cell purchased from Hartl lab at the University of Reading, UK.[85] The OTTLE cell was equipped with a gold mesh working electrode, a platinum-mesh counter electrode, and a silver-foil pseudoreference electrode in CaF_2 windows. The same solvent and electrolyte system used for the cyclic voltammetric experiments was used for the spectroelectrochemistry studies.

3. X-ray Crystallographic Analysis. Single crystals were mounted in a thin-walled glass capillary on an Enraf-Noius CAD-4 diffractometer at 25 °C using graphite-monochromated Mo Kα radiation (λ = 0.71073 Å). Unit cell parameters were determined by least-squares analysis of 25 reflections. The intensity data were collected in the ω/2θ scan mode and three standard reflections were monitored every hour during data collection. The data were corrected for Lorentz-polarization effects, decay, and empirical absorption corrections when ψ-scans were applied. The structure was solved using the Patterson method and refined by full-matrix least squares techniques on F^2 using the SHELXS-97 and SHELXL program packages.[86-87] The final structures were confirmed by anomalous dispersion effects with Friedel pairs, which were not merged. All non-hydrogen atoms were refined anisotropically except for disordered atoms. All hydrogen atoms were refined and positioned geometrically using the riding model with fixed isotropic thermal factors. The crystallographic data and refinements are summarized in Table 1. The CCDC reference numbers are 1914650 - 1914652.

4. Computational Methods. All calculations were carried out using the Gaussian 16 program package (A.03 version).[88] Geometries corresponding to the stationary points on the ground state potential energy surface of all structures were fully optimized using density functional theory (DFT) with a range-separated hybrid functional and dispersion corrections (LC-wPBE-D3).[89-93] All calculations were performed using the Karlsruhe basis sets developed by Ahlich et al. at the triple-ζ level (def2TZVP). Charged states were considered open shell with doublet and triplet spin states for the mono-cationic and the dicationic species, respectively. The solvent environment was modeled as a dielectric continuum using a self-consistent reaction field (SCRF)[94-96] approach and conductor-like polarizable continuum model (CPCM)[97-98] in CH_2Cl_2. Vibrational frequency calculations were performed to confirm the energy minima of the optimized stationary points and to extract the IR frequencies and intensities. The excitation energies and oscillator strengths for the monocationic mixed valence systems at their optimized geometries in the ground state were obtained by linear response time-dependent density functional theory (TD-DFT) calculations employing the PBE0 hybrid functional and def2TZVP basis set.[99-100] Natural transition orbital (NTO)[101] analyses were performed to identify the nature of the nature of the electronic transitions evident for the MVSs.

Results and Discussion

Synthesis and Structural Geometries

Synthetic protocols that exploit Pd-catalyzed Negishi or Suzuki-Miyaura reactions, and a 1,8-naphthyl pillaring motif previously reported for the synthesis of π-stacked porphyrin-bridge-quinone systems, were used to construct three neutral precursor molecules, 1,8-bis(2',5'-dimethoxybenzene-1'-yl)naphthalene (**1**), 1,4-bis(8'-(2",5"-dimethoxybenzene-1"-yl)naphthalen-1'-yl)benzene (**2**), and 1,8-bis(4'-(8"-(2"',5"'-dimethoxybenzene-1"'-yl)naphthalen-1"-yl)benzene-1'-yl)naphthalene (**3**).[30,102-103] The synthetic schemes are summarized in the Supporting Information (Scheme S1). These supramolecular structures were fully characterized by ^{1}H- and ^{13}C-NMR, high-resolution mass spectroscopy, and

electronic absorption spectroscopy. Two-dimensional NMR spectra (COSY) were additionally acquired for **2** and **3** in order to fully assign all resonances.

The three-dimensional geometries of these molecules were determined by X-ray crystallography. Single crystals of compound **1** suitable for X-ray crystallographic analysis were obtained via slow evaporation of a saturated hexane solution, which was prepared at 65 °C and subsequently cooled slowly to 25 °C. Unfortunately, the same methods could not be applied to compound **2** and **3** due to their low solubility in nonpolar hexane. Single crystals of compound **2** were grown in a closed chamber from a saturated THF solution in the presence of hexane vapor, while those of compound **3** were grown via slow evaporation of a CH_2Cl_2/hexane solution at 25 °C. Crystal data, details regarding the data collection, and refinement parameters are listed in Table 1. ORTEP drawings with atomic labelling for nonhydrogen atoms, refined positional parameters, positional parameters for hydrogens, refined thermal parameters, selected bond distances, and angles are listed in SI (Tables S1-S14, Figures S10-S12).

Table 1. Crystal data and structure refinements of **1**, **2**, and **3**.

	1	**2**	**3**
Empirical formula	$C_{52}H_{48}O_8$	$C_{42}H_{34}O_4$	$C_{58}H_{44}O_4$
Formula weight	800.90	602.69	804.93
Temperature (K)	100	143	100
Crystal system	triclinic	monoclinic	triclinic
Space group	$P\bar{1}$	$P2_1/n$	$P\bar{1}$
Unit cell dimensions			
a (Å)	10.3501(7)	8.5838(13)	10.2051(7)
b (Å)	14.2207(9)	10.115(2)	14.0657(9)
c (Å)	15.2690(10)	18.403(3)	14.7693(10)
α (°)	80.734(2)		93.402(2)
β (°)	74.952(2	98.6370(10)	97.526(2)
γ (°)	69.762(2)		103.089(2)
Volume ($Å^3$),	2030.0(2)	1579.8(4)	2038.4(2)
Z	2	2	2
Density (calculated) (Mg/m^3)	1.310	1.267	1.311
Absorption coefficient (mm^{-1})	0.087	0.080	0.081 [1]
F(000)	848.0	636	848.0
Crystal size (mm)	0.17 × 0.11 × 0.07	0.40 x 0.10 x 0.10	0.24 × 0.24 × 0.05
2θ range for data collection (°)	6.024 - 50.82°	5.6 – 50.7 °	5.898 - 50.88
Index ranges	$-12 \le h \le 12$	$-8 \le h \le 10$	$-12 \le h \le 12$

	-17 ≤ k ≤ 17	-12 ≤ k ≤ 10	-17 ≤ k ≤ 16
	-18 ≤ l ≤ 18	-22 ≤ l ≤ 17	0 ≤ l ≤ 17
Reflections collected	42324	9096	52569
Independent reflections	7457[R(int) = 0.0877]	2875[R(int) = 0.0256]	7494[R(int) = 0.0483]
Data/restraints/parameters	7457/0/549	2875/0/210	7494/956/793
Goodness-of-fit on F2	1.073	1.074	1.135
Final R indexes [I>=2σ (I)]	R_1 = 0.0692, wR_2 = 0.1581	R_1=0.0573, wR_2=0.1357	R_1 = 0.0838, wR_2 = 0.1732
Final R indexes [all data]	R_1 = 0.1022, wR_2 = 0.1752	R_1=0.0796, wR_2=0.1539	R_1 = 0.1120, wR_2 = 0.1894
Largest diff. peak/hole (eÅ^{-3})	0.45/-0.39	+0.213/-0.247	0.46/-0.52

It is worth noting that compounds **1**, **2**, and **3** can form diastereomeric mixtures generated by the relative orientations of the termnal $\mathbf{D_1}$ and $\mathbf{D_2}$ units (*syn* or *anti*) and the tilting direction of the 1,8-naphthyl pillaring motif relative to the virtually orthogonal **D** or phenylene ring plane (/ or \). A simple method to assign diastereomers is shown in Figure 2; these diastereomers are also schematically illustrated in Figures 3 and 4.

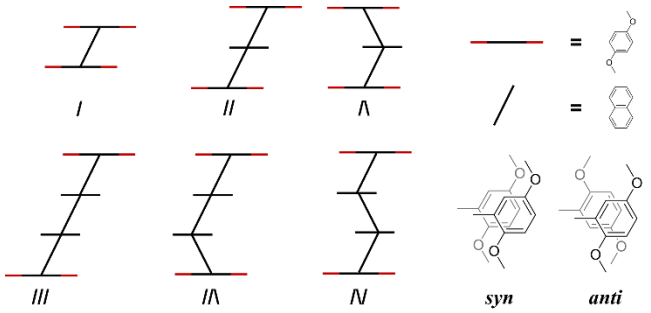

Figure 2. Schematically illustrating the different conformations of compounds **1**, **2**, and **3**.

The geometry of neutral compound **1**, determined by X-ray crystallography, gave rise to two crystallographically independent molecules. The geometrical parameters of each are slightly different, but the overall shape of the molecule can be designated as **1_*anti*_/** (Figure 3). When two **D** groups are cofacially aligned in a juxtaposed manner, the *anti* orientation dominates due to the steric hindrance between methoxy groups belonging to the different **D** groups. The ^{1}H-NMR spectroscopic data demonstrate that the relative occupancies of the *syn*/*anti* conformers are 13/87 in solution at ambient temperature. The dihedral angles between **D** and the naphthalene ring planes ranged from 80.9-85.4°; $\mathbf{D_1}$ and $\mathbf{D_2}$ were attached to the 1,8-positions of the naphthyl pillar in a virtually orthogonal manner, thus the extent of tilting of the naphthyl pillar was only minor. Two **D** groups were slightly laterally shifted from

a perfectly eclipsed juxtaposed position. The centroid-to-centroid distance between $\mathbf{D_1}$ and $\mathbf{D_2}$ was 3.40 Å.

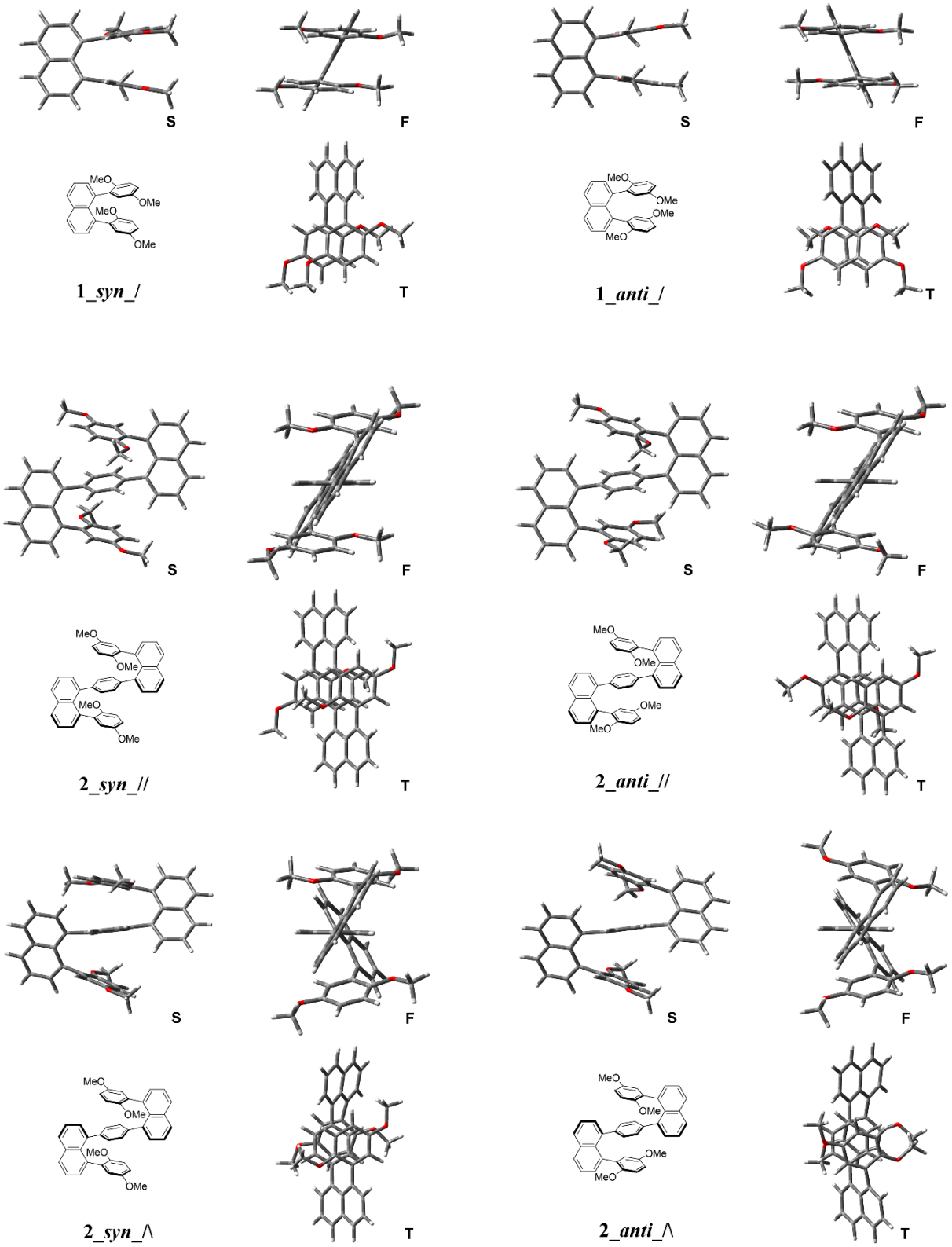

Figure 3. Front (F), side (S), and top (T) views of different conformations of **1** and **2**.

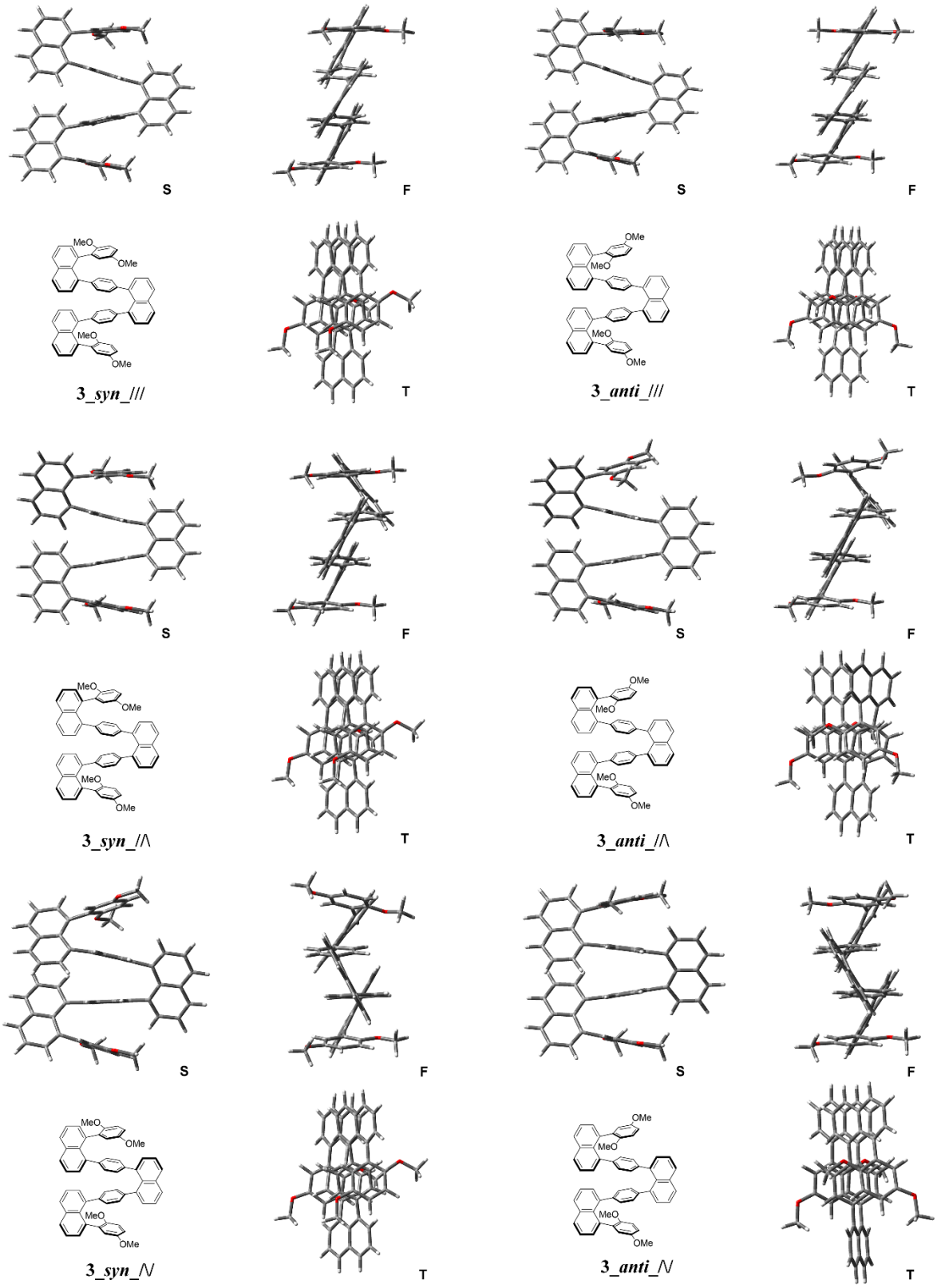

Figure 4. Front (F), side (S), and top (T) views of different conformations of **3**.

In the case of compound **2**, the steric hindrance between the two methoxy groups was largely diminished, due to the sandwiched phenylene spacer separating the two **D** groups, such that two orientations, *syn* and *anti*, are both accessible. NMR spectroscopic data show that virtually equal amounts of both *syn* and *anti* orientations co-exist in the solution phase. The proton peaks in the aromatic region of the *syn* and *anti* conformations were not distinguishable. However, the presence of both conformations was confirmed by two pairs of methoxy peaks, observed at 3.689/3.298 and 3.537/3.44 in the ^{1}H-NMR spectrum, where peaks corresponding to each conformation were clearly resolved.

The geometry observed by X-ray crystallography was nonetheless the *syn* orientation. In terms of the two naphthyl pillars, they were parallel to each other establishing a // arrangement. Interestingly, dihedral angles between **D** and the naphthalene ring planes were within the 60.6-62.5° range, while those between naphthalene and phenylene ring planes were 58.5° to 60.5°. Compared to compound **1**, these dihedral angles are more than 20° smaller: thus the naphthalene pillars in compound **2** are more tilted, and the lateral shift of juxtaposed aromatic units is larger. The centroid-to-centroid distance between $\mathbf{D_1}$ (or $\mathbf{D_2}$) and the nearby phenylene spacer was 3.57 Å and is longer than that between the two **D** groups in compound **1**. Due to the // arrangement of the two naphthyl pillars, the centroid-to-centroid distance between $\mathbf{D_1}$ and $\mathbf{D_2}$ was simply the sum of the two individual centroid-to-centroid distances between **D** and the nearby phenylene spacer (7.14 Å).

The crystals of compound **3** grew as non-merohedral twins, which gave two disordered **D** groups in two different orientations. This feature, anticipated for compound **2** yet not observed by crystallography, was indeed resolved in the crystal structures for compound **3**. Although the relative occupancies of *syn*/*anti* conformers determined by X-ray crystallography were 80/20, they were approximately 50/50 in the solution phase according to ^{1}H- and ^{13}C-NMR spectroscopic data. The arrangement of three naphthyl pillars was found to be //\, out of the three possibilities including ///, //\, and /\/.

Values of dihedral angles in compound **3** are similar, though span a slightly broader range, relative to those observed in compound **2**. The dihedral angles between **D** and the naphthalene ring plane were in the range of 61.8-67.3° and those between naphthalene and the phenylene ring plane were between 51.4°

and 63.1°. The respective centroid-to-centroid distances are 3.52, 3.79, and 3.45 Å for the **D_1**-phenylene spacer separation, that between the two phenylene spacers, and the **D_2**-phenylene spacer separation, in the **3_*syn*_**//\ arrangement. Those for the corresponding **3_*anti*_**//\ conformer were 3.48, 3.79, and 3.42 Å. Due to the //\ arrangement of the three naphthyl pillars, the two phenylene spacers were shifted laterally from **D_1** to one side, with the capping **D_2** moiety shifted to the other side. **D_1** and **D_2** were thus placed in a vertically superimposed position. The centroid-to-centroid distances between **D_1** and **D_2** were found to be 10.25 and 10.42 Å for **3_*syn*_**//\ and **3_*anti*_**//\, respectively, which are shorter than the sum of the three individual centroid-to-centroid distances.

It is important to note that the distances between the **D_1** and **D_2** redox centers determined here (3.40, 7.14, and 10.33, the average value of 10.25 and 10.42 Å), cannot be used directly as geometrical parameters for the distance dependence of electronic couplings because the MVSs of interest involve the monocation radical versions of these neutral compounds. The **D_1-D_2** distances are /expected to diminish upon one electron oxidation. Since crystallographic data for the monocationic species were not available, we performed DFT calculations to obtain the required geometrical information. We used the crystal structures of **1_*anti*_**/, **2_*syn*_**//, **3_*syn*_**//**,** and **3_*anti*_**//\ as starting geometries for optimizing the structures of the neutral, monocationic, and dicationic species. Geometric optimizations of **1_*syn*_**/ and **2_*anti*_**// were also performed. The starting geometries were prepared by fixing dihedral angles between **D** and the naphthalene ring planes of **1_*anti*/** and **2_*syn*_**//.

In order to reproduce the molecular structures of compounds **1**-**3**, as well as compute those corresponding to their monocationic and dicationic charged states by DFT methods, it is important to consider long-range London dispersion interactions. In our recent work on the fractional crystallization behavior of 1-(pyridine-2-yl)ethylamine, the employment of the DFT-D3 method developed by Grimme,[90-93] which includes a pairwise interaction to overcome the intrinsic lack of dispersion interactions, was verified to be useful for reproducing the three dimensional crystal structures and calculating cohesive energies. On the other hand, one of the major problems encountered in the calculations for MVSs by the DFT approach is an overly delocalized description caused by a self-

interaction error. This error can be reduced by increasing the amount of exact-exchange admixture in the hybrid function.[104] With this information in hand, we performed geometric optimizations of compound **2** in both neutral and monocationic states by screening 16 different density functionals, both with and without dispersion correction. The range-separated LC-wPBE with dispersion correction (LC-wPBE-D3) approach was found to be the most reliable method in terms of the important geometrical parameters that include the centroid-to-centroid distance between $\mathbf{D_1}$ and $\mathbf{D_2}$ and dihedral angles between **D** (or phenylene spacer) and naphthyl ring planes. The details of the screening processes used are beyond the scope of this manuscript and thus will be discussed elsewhere.

Table 2. Comparison of Geometrical Parameters.[a]

Conformation	X-ray		DFT	
	$d^0_{cryst.}$	$d^{\bullet+}_{MVS}$[a]	$d^0_{calc.}$	$d^{\bullet+}_{calc.}$
1_***syn***_/		3.29	3.37	3.21
1_***anti***_/	3.40		3.45	3.34
2_ ***syn*** _//	7.14		6.96	6.90
2_ ***syn*** _/\		7.01	6.90	6.63
2_ ***anti***_//			6.90	6.83
2_ ***anti***_/\			6.88	6.76
3_***syn***_///			10.43	10.29
3_***syn***_/\	10.25		9.94	9.82
3_***syn***_/\/		10.13	9.80	9.65
3_ ***anti*** _///			10.51	10.41
3_ ***anti*** _/\	10.42		10.15	10.07
3_ ***anti*** _/\/			9.61	9.51

[a]Estimated values of centroid-to centroid distance between two dimethoxybenzene rings in the cationic MVS by the relation $d^{\bullet+}_{MVS} = d^0_{cryst.} - (d^0_{calc.} - d^{\bullet+}_{calc.})$

The centroid-to-centroid distances between $\mathbf{D_1}$ and $\mathbf{D_2}$ determined by X-ray crystallography ($d^0_{cryst.}$) along with those by DFT calculations ($d^0_{calc.}$ and $d^{\bullet+}_{calc.}$) are listed in Table 2. Upon one-electron oxidation, the centroid-to-centroid distance between $\mathbf{D_1}$ and $\mathbf{D_2}$ of **1_anti_/** was computed to decrease by *ca.* 5%. The decrease for (**2_ syn _//**)$^{\bullet+}$ relative to **2_ syn _//** was found to be minor (~1%). The $d^{\bullet+}_{calc.}$ value for **3_syn_/Λ** was also slightly shorter than the corresponding $d^0_{calc.}$ value (~1%). The $\mathbf{D_1}$-$\mathbf{D_2}$ distances for the three MVSs ($d^{\bullet+}_{MVS}$) were estimated by considering the trend revealed by these computations and crystallographically determined d^0_{cryst} values, and are listed in the third column of Table 2.

Electrochemistry

Potentiometric data for compounds **1**, **2**, and **3** were determined from cyclic voltammetric experiments (CV) carried out in a CH_2Cl_2/CH_3CN solvent mixture (3:2) containing 0.1 M tetrabutylammonium hexafluorophosphate ($TBAPF_6$) as the electrolyte at 25 °C (Figure 5). The cyclic voltammetric response of compound **1** shows two non-reversible, yet distinct and resolved, anodic waves at approximately 0.8 and 1.1 V versus the Fc/Fc^+ internal reference. That of compound **3**, however, shows a quasi-reversible unresolved anodic wave at ~0.7 V. The voltammetric response of compound **2** displays characteristics that lie in between those determined for **1** and **3**, having an overall shape close to a reversible wave, but with the presence of a shoulder peak between the anodic and the cathodic peak potentials, indicating that two anodic waves are overlapped. The currents measured for compound **2** and **3** using CV methods were virtually identical, implying that the anodic wave observed for compound **3** is also a 2e process. In order to obtain more precise oxidation potentials for these compounds, we carried out corresponding differential pulse voltammetric (DPV) measurements. The oxidation potentials of compound **1** were clearly resolved at E°_{ox} = 0.72 and 1.02 V vs the Fc/Fc^+ couple. The oxidation potentials for **2** and **3** were analyzed by Gaussian deconvolution to obtain E°_{ox} = 0.67 and 0.78 V, and E°_{ox} = 0.70 and 0.80 V vs the Fc/Fc^+ couple, respectively, for these compunds (Table 3).

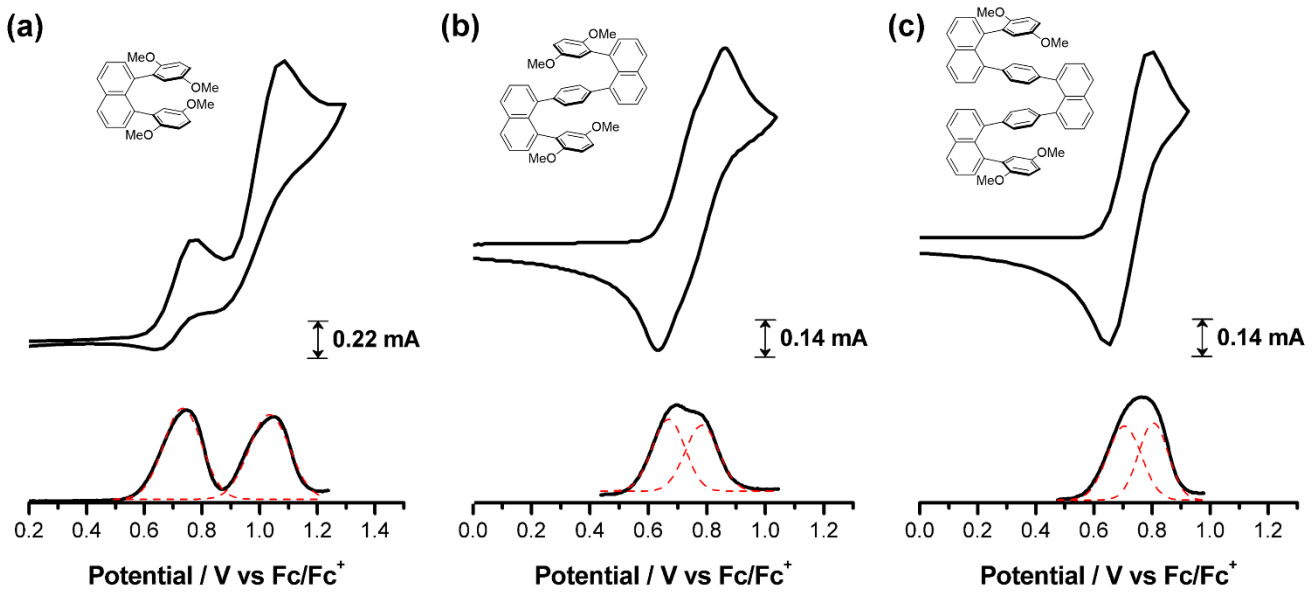

Figure 5. Cyclic voltammetric (top) and differential pulse voltammetric responses (with Gaussian deconvolution, bottom) of (a) **1**, (b) **2**, and (c) **3**. Experimental conditions: [compound] = 4 mM (2 mmol for **1**); [$TBAPF_6$] = 0.1 M; solvent = CH_2Cl_2:CH_3CN = 3:2; temperature = 25 °C; scan rate = 180 mV/s; reference electrode = Ag/Ag^+; working electrode = glassy carbon. All potentials are referenced to a Fc/Fc^+ couple as an internal standard.

Table 3. Differential Pulse Voltammetric Data.[a]

Complex	E_{ox1}	E_{ox1}	ΔE_{ox}
		V vs Fc/Fc^+	
1	0.72	1.02	0.30
2	0.67	0.78	0.11
3	0.70	0.80	0.10

[a]Experimental conditions: [compound] = 4 mM; [$TBAPF_6$] = 0.1 M; solvent = CH_2Cl_2:CH_3CN = 3:2; temperature = 25 °C; scan rate = 180 mV/s; reference electrode = Ag/Ag^+; working electrode = glassy carbon. All potentials are referenced to a Fc/Fc^+ couple as an internal standard.

A fundamental question arises regarding the origin of the oxidation potentials being due to $\mathbf{D_1}$ and $\mathbf{D_2}$, naphthalene(s), or both. Since the aim of this work is to quantify electronic coupling through π-stacked aromatic units, the involvement of the naphthalene unit in these anodic redox processes would define a

pitfall in the design of these MVS structures. Literature values of oxidation potentials for both **D** and naphthalene are coincidentally identical (1.34 V vs Ag/Ag^+), thus the origin of the oxidation potentials observed via electrochemical experiments would be ambiguous. To resolve this potential issue, we examined the frontier molecular orbitals (MOs) of the three compounds, obtained from DFT calculations. In Figure 6, the energy levels of the five frontier occupied MOs of **1**, **2**, and **3** in neutral states are shown along with their respective 3-dimensional isosurfaces. In all three compounds, both the HOMO and HOMO-1 are mainly localized on one or two **D** groups. The HOMO energy levels of free dimethoxybenzene and naphthalene, which were also obtained via DFT calculations, are compared using dotted lines in Figure 6. Note that the HOMO energy levels of **1**, **2**, and **3** are even more negative than that of free dimethoxybenzene, by *ca*. 0.16 eV, due to the destabilization caused by significant π-cofacial interactions. Moreover, HOMO-1 orbitals are at least 0.11 eV more negative than HOMO-2 orbitals in which dominant populations are localized on one or two naphthalene units. These results safely exclude the possibility of scrambling the venue for the first oxidation, and therefore ensure that anodic redox processes probed in the Figure 5 data reflect $\mathbf{D_1}$-centered oxidations in all three compounds.

The 3-dimensional isosurfaces of the SOMOs of $\mathbf{1^{\bullet+}}$, $\mathbf{2^{\bullet+}}$, and $\mathbf{3^{\bullet+}}$ MVSs are shown in Figure 7. The electron densities of the SOMOs of the three monocationic MVSs are substantially localized on the $\mathbf{D_2}$ moiety. These features were further illuminated using a spin density diagram (Figure 7). The shapes of both SOMO and spin density isosurfaces are quite similar each other congruent with a $\mathbf{D_1}$-localized first oxidation.

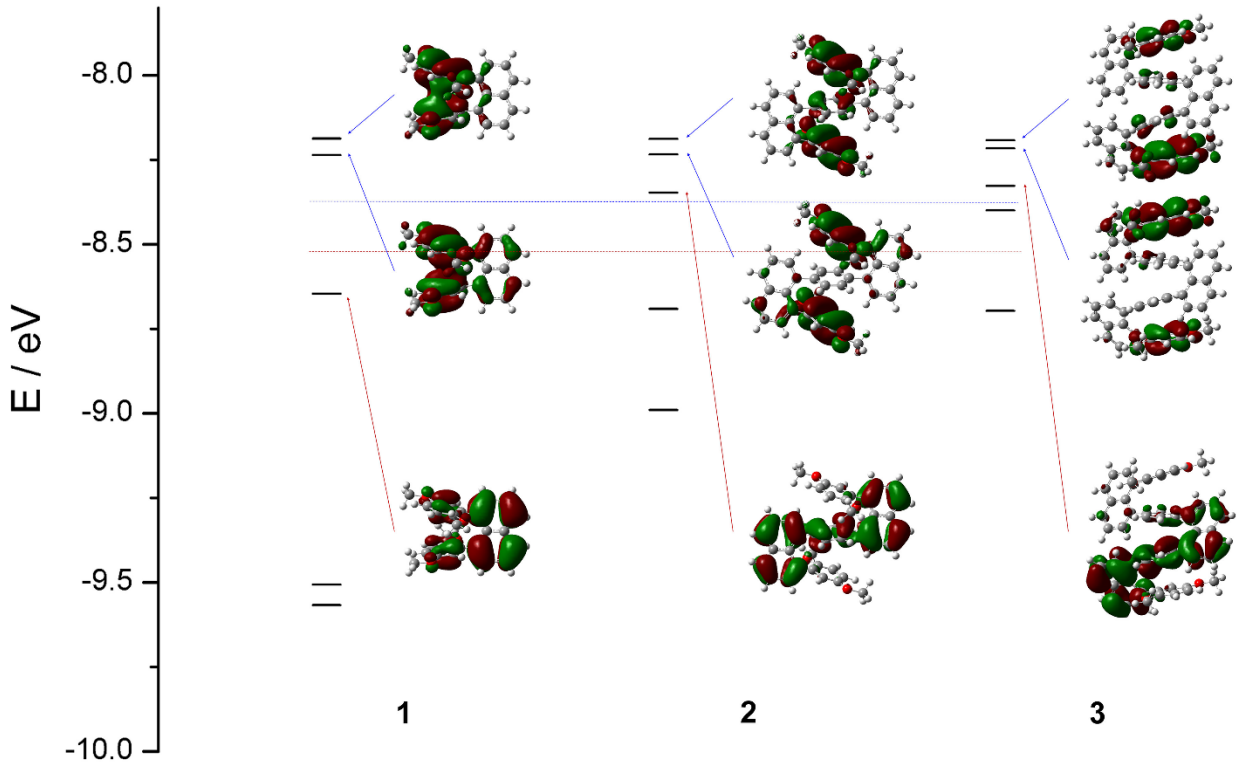

Figure 6. Energies of occupied frontier molecular orbitals of three representative MVSs, **1**_***anti***_/ (**1**), **2**_***syn***_// (**2**), **3**_***syn***_//\ (**3**), at the LC-wPBE-D3/def2TZVP level. The HOMO energy levels of free dimethoxybenzene (-8.37 eV) and naphthalene (-8.53 eV) molecules are noted by the respective blue and red dotted lines. Note that both HOMO and HOMO-1 orbitals of all three MVSs are mainly localized in dimethoxybenzene moieties.

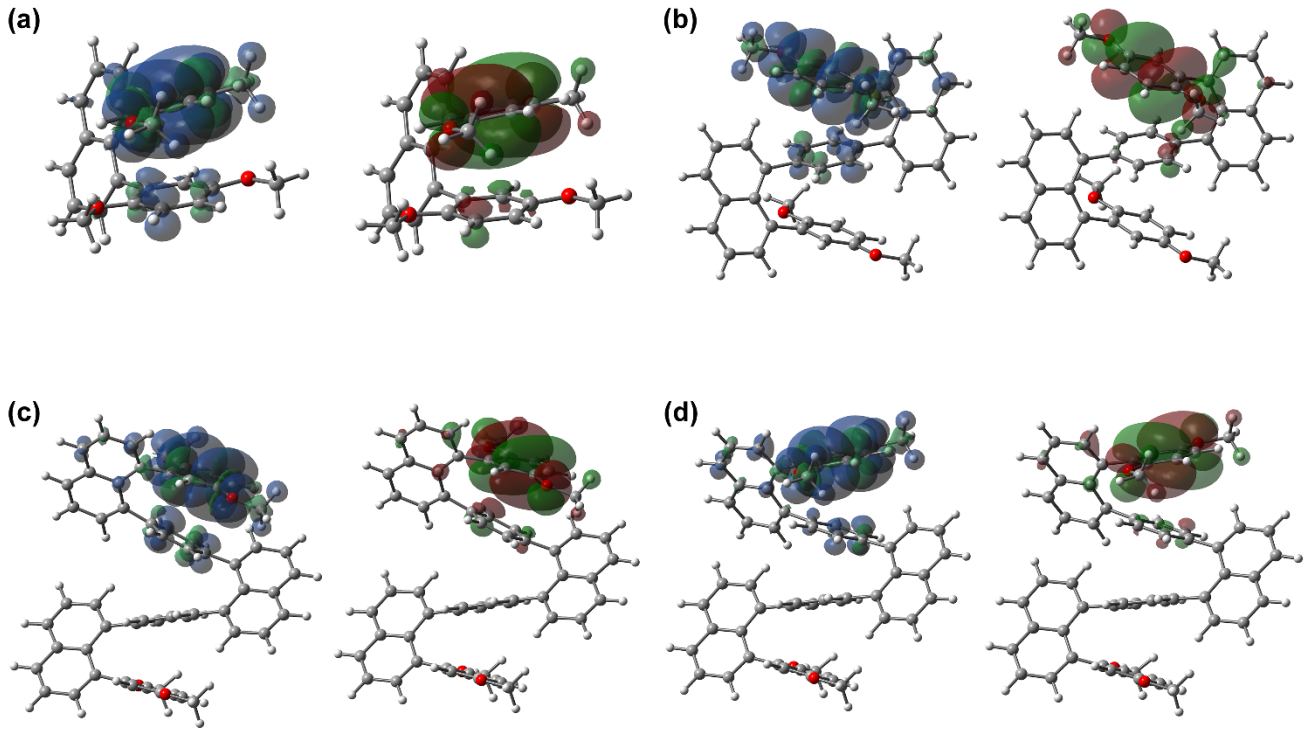

Figure 7. Similarities between spin density (left) and β-spin SOMO (right) isosurfaces (±0.02 a.u.) of (a) **[1_*anti*_/]**$^{\bullet+}$, (b) **[2_*syn*_//]**$^{\bullet+}$, (c) **[3_*syn*_//\]**$^{\bullet+}$, and (d) **[3_*anti*_//\]**$^{\bullet+}$ as obtained at the LC-wPBE/def2TZVP level. Conformations of DMB relative orientations (*syn*/*anti*) as well as naphthalene pillaring motives (/, //, and //\) are based on the X-ray crystallographic data.

Since the approaches to determine electronic coupling values from electronic absorption data are different for class II and class III MVSs (Figure 1), an appropriate Robin-Day classification is critical for the extraction of accurate electronic coupling values from experiment data. As illustrated in Figure 1, charge is completely delocalized over two redox centers in a class III MVS: the two redox centers are thus symmetrical. On the other hand, such symmetry is broken in class II MVSs. These features are manifested in geometrical parameters, most notably in bond lengths. Kochi and coworkers reported X-ray crystallographic data of a series of MVSs that used 4-methyl-2,5-dimethoxybenzenes as redox centers.[82-83,105] The MVSs exhibited characteristic quinonoidal distortions of dimethoxybenzene redox centers upon 1e oxidation from their centrosymmetric benzenoid geometries in their neutral state (Figure 8). Two sets of five α-ε bond lengths in monocationic dimethoxybenzene compounds (Figure 8), for example, 4,4'-dimethyl-2,2',5,5'-tetramethoxy-1,1'-biphenyl[82,105] or 1,2-bis(2,5-dimethoxy-4-methyltolyl)tetramethylbenzene,[83] were indeed virtually identical to each other, indicating that these

compounds belong to class III MVSs. Such geometrical parameters of corresponding dimethoxybenzenes in class II MVSs showed small but apparent differences.

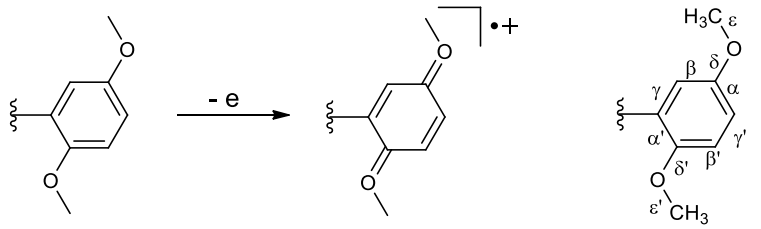

Figure 8. Left: quinonoidal distortions of dimethoxybenzene upon 1e oxidation; right: bond specification scheme.

A similar analysis was applied to $\mathbf{1}^{\bullet+}$, $\mathbf{2}^{\bullet+}$, and $\mathbf{3}^{\bullet+}$. In lieu of crystallographic data for these monocationic species, we took advantage of the DFT computational results. Two sets of five α-ε bond lengths in $\mathbf{D_1}$ and the $\mathbf{D_2}$ moieties including both *syn* and *anti* conformations are listed in Table 4. Despite the fact that DFT analysis tends to provide a delocalized charge distribution in general,[104] the results showed that α-ε bond lengths of $\mathbf{D_1}$ in all 6 geometries differ clearly from those of their $\mathbf{D_2}$ counterparts. The three MVSs studied in this work are therefore classified as class II and thus electronic coupling values can be calculated using Eq.2.

Table 4. Geometrical Parameters of the Dimethoxybenzene Moieties in the MV systems obtained from DFT calculations.[a]

MVS	L	α/α'	$\beta\beta'$	γ/γ'	δ/δ'	ε/ε'	ζ	H (cm^{-1})
[1_*syn*_/]$^{\bullet+}$	D_1	1.381/1.389 [1.385]	1.404/1.380 [1.392]	1.377/1.389 [1.383]	1.356/1.357 [1.357]	1.412/1.412 [1.412]	4.763×10^{-2}	3739
	D_2	1.413/1.414 [1.413]	1.435/1.416 [1.425]	1.352/1.355 [1.354]	1.301/1.305 [1.303]	1.431/1.432 [1.431]	9.578×10^{-1}	3528
[1_*anti*_/]$^{\bullet+}$	D_1	1.381/1.390 [1.385]	1.398/1.379 [1.389]	1.376/1.391 [1.383]	1.356/1.358 [1.357]	1.412/1.413 [1.413]	3.608×10^{-2}	3274
	D_2	1.415/1.414 [1.414]	1.436/1.416 [1.426]	1.351/1.354 [1.353]	1.300/1.305 [1.303]	1.434/1.432 [1.433]	9.673×10^{-1}	3123
[2_*syn*_//]$^{\bullet+}$	D_1	1.400/1.378 [1.389]	1.378/1.390 [1.384]	1.391/1.376 [1.384]	1.357/1.360 [1.358]	1.410/1.410 [1.410]	7.517×10^{-3}	1371
	D_2	1.414/1.413 [1.413]	1.436/1.416 [1.426]	1.352/1.355 [1.354]	1.300/1.305 [1.302]	1.432/1.432 [1.432]	9.877×10^{-1}	1748
[2_*anti*_//]$^{\bullet+}$	D_1	1.400/1.379 [1.390]	1.379/1.389 [1.384]	1.390/1.375 [1.383]	1.359/1.358 [1.359]	1.410/1.411 [1.410]	8.693×10^{-3}	1474
	D_2	1.413/1.413 [1.413]	1.436/1.416 [1.426]	1.353/1.355 [1.354]	1.300/1.305 [1.302]	1.432/1.432 [1.432]	9.888×10^{-1}	1668

[2_ *syn* _/|]$^{\bullet+}$	D_1	1.378/1.400 [1.384]	1.390/1.378 [1.384]	1.376/1.390 [1.388]	1.360/1.357 [1.358]	1.411/1.410 [1.410]	1.402×10^{-2}	1867
	D_2	1.416/1.434 [1.425]	1.414/1.415 [1.414]	1.351/1.354 [1.353]	1.304/1.301 [1.302]	1.432/1.432 [1.432]	9.855×10^{-1}	1899
[2_ *anti* _/|]$^{\bullet+}$	D_1	1.379/1.400 [1.389]	1.390/1.378 [1.384]	1.375/1.391 [1.383]	1.359/1.359 [1.359]	1.410/1.410 [1.410]	1.059×10^{-2}	1179
	D_2	1.416/1.435 [1.425]	1.414/1.415 [1.414]	1.352/1.354 [1.353]	1.304/1.301 [1.303]	1.432/1.432 [1.432]	9.945×10^{-1}	1625
[3_*syn*_///|]$^{\bullet+}$	D_1	1.378/1.400 [1.389]	1.390/1.378 [1.384]	1.376/1.391 [1.384]	1.360/1.357 [1.359]	1.410/1.409 [1.410]	1.081×10^{-2}	678
	D_2	1.413/1.435 [1.424]	1.413/1.415 [1.414]	1.352/1.354 [1.353]	1.304/1.301 [1.302]	1.433/1.432 [1.432]	9.980×10^{-1}	1567
[3_ *anti* _///|]$^{\bullet+}$	D_1	1.378/1.400 [1.389]	1.390/1.378 [1.384]	1.376/1.391 [1.384]	1.360/1.357 [1.359]	1.410/1.409 [1.410]	3.966×10^{-3}	952
	D_2	1.416/1.436 [1.426]	1.413/1.413 [1.413]	1.352/1.355 [1.354]	1.305/1.300 [1.302]	1.432/1.432 [1.432]	9.979×10^{-1}	696
[3_*syn*_/|]$^{\bullet+}$	D_1	1.378/1.400 [1.389]	1.390/1.378 [1.384]	1.376/1.391 [1.384]	1.360/1.357 [1.359]	1.410/1.409 [1.410]	2.227×10^{-3}	714
	D_2	1.412/1.414 [1.413]	1.436/1.415 [1.425]	1.352/1.354 [1.353]	1.301/1.304 [1.303]	1.431/1.435 [1.433]	9.972×10^{-1}	796
[3_ *anti* _/|]$^{\bullet+}$	D_1	1.378/1.399 [1.389]	1.390/1.378 [1.384]	1.376/1.391 [1.384]	1.360/1.357 [1.359]	1.410/1.409 [1.410]	1.699×10^{-3}	624
	D_2	1.416/1.436 [1.426]	1.413/1.415 [1.414]	1.353/1.354 [1.353]	1.305/1.301 [1.303]	1.432/1.433 [1.432]	9.944×10^{-1}	1133
[3_*syn*_/\/|]$^{\bullet+}$	D_1	1.378/1.400 [1.389]	1.389/1.378 [1.384]	1.376/1.391 [1.383]	1.360/1.357 [1.359]	1.410/1.409 [1.410]	4.161×10^{-3}	975
	D_2	1.416/1.435 [1.426]	1.413/1.415 [1.414]	1.352/1.354 [1.353]	1.304/1.301 [1.303]	1.432/1.433 [1.432]	9.976×10^{-1}	743
[3_ *anti* _/\/|]$^{\bullet+}$	D_1	1.378/1.400 [1.389]	1.389/1.378 [1.384]	1.376/1.390 [1.383]	1.361/1.357 [1.359]	1.410/1.409 [1.410]	8.257×10^{-3}	1371
	D_2	1.416/1.436 [1.426]	1.413/1.412 [1.413]	1.352/1.355 [1.353]	1.305/1.301 [1.303]	1.433/1.431 [1.432]	9.970×10^{-1}	835

[a]Average bond lengths (Å) in brackets. [b]Dimethoxybenzene moieties possessing less positive charge (D_1) and more positive charge (D_2). [c]Charge-resonance contribution evaluated by eq.5. [d]Electronic coupling matrix element evaluated according to eq. 5. See Table 5 for the ΔE values of the systems.

An interesting outcome of Kochi's work was that charge-resonance contributions (ζ) could be calculated reliably by linear regression of geometrical parameters using the following equation.

$$\zeta_i = (d_0 - d_i)/(d_0 - d_1) \qquad \text{(eq. 6)}$$

In eq. 6, ζ_i is the partial charge component over the designated bond, d_0 and d_1 are the bond lengths in the neutral and the one-electron oxidized states, respectively, and d_i is the pertinent bond length in a redox-center of the mixed-valence cation. Similar analyses were performed for our three MVSs with geometrical parameters obtained from DFT calculations. We adopt d_0 and d_1 values from the neutral and dicationic species of **1**-**3**, respectively, and d_i values from their monocationic species. The geometrical parameters of the neutral and dicationic species of **1**-**3** are listed in Tables S27 and S28, respectively. Unlike Kochi's

work, in which only the exocyclic δ bond was used to derive ζ_i values, we considered all five bonds, including three endocyclic bond lengths (α-γ) and two exocyclic ones (δ and ε) for the two dimethoxybenzene rings of each MVS. The ζ values were thus averaged over five individual ζ_i values. Electronic coupling matrix elements were then evaluated with these ζ values according to eq. 5 and listed in the last column of Table 4. A discussion of these electronic coupling values and their distance dependence follows below.

Spectroelectrochemistry

The UV/vis/NIR electronic absorption spectra of monocationic MVSs were monitored spectroelectrochemically using an OTTLE cell.[85] From an intial potential of 0.4 V vs a silver foil pseudo-reference electrode (~0.3 V vs Fc/Fc^+), the potential of the gold mesh working electrode was gradually increased at a +5 mV/s sweep rate. Corresponding spectroelectrochemical data are shown in Figure 9. The lowest energy absorption bands of neutral compounds **1**-**3** reside near 300 nm due to the absorption of **D**. As spectra were acquired at increasing positive potential, new absorption bands appeared in the 400–900 nm range. The spectral data acquisition window used in these experiments spanned through 2500 nm, but all three compounds remained optically transparent above 1000 nm. Newly emerged electronic absorption manifolds for the three MVSs exhibited two band maxima at 464/572, 478/606, and 461/659 nm for $\mathbf{1}^{\bullet+}$, $\mathbf{2}^{\bullet+}$, and $\mathbf{3}^{\bullet+}$, respectively. While the higher energy absorptions for $\mathbf{1}^{\bullet+}$, $\mathbf{2}^{\bullet+}$, and $\mathbf{3}^{\bullet+}$ occur at similar wavelengths, those corresponding to the lower energy absorptions clearly depend on molecular size. In order to determine whether these bands are absorption bands of naphthalene or **D** cation radicals, we performed spectroelectrochemistry of dimethoxybenzene and naphthalene separately (Figure S18). The lowest energy absorption band of the naphthalene cation radical is centered at 548 nm; the dimethoxybenzene cation radical exhibits multiple distinct absorptions in the visible region between 436 and 461 nm of similar intensity, as well as a very broad band having and order of magnitude smaller extinction coefficient centered at 615 nm. These absorption bands were compared with those of our MVSs and are displayed as arrows with distinct colors and line styles in Figure 9. Note that the energies of these

absorption manifolds are not coincident with those of $\mathbf{1}^{\bullet+}$, $\mathbf{2}^{\bullet+}$, and $\mathbf{3}^{\bullet+}$; thus the lowest energy red-shifted bands of these MVSs cannot be associated with the cation radical absorptions of naphthalene and dimethoxybenzene: the $\mathbf{1}^{\bullet+}$, $\mathbf{2}^{\bullet+}$, and $\mathbf{3}^{\bullet+}$ low energy absorptions thus demark IVCT bands.

In order to evaluate the IVCT character of these transitions further, we performed TD-DFT calculations for the three representative MVS sytems, **[1_*anti*_/]**$^{\bullet+}$, **[2_*syn*_//]**$^{\bullet+}$, and **[3_*syn*_//\]**$^{\bullet+}$. We employed the same DFT level of theory used for the geometry optimizations but the DFT functional was changed to PBE0-D3 because LC-wPBE-D3 could not properly describe the natures of the electronic transitions. For each of the above geometries, we calculated 10 excited states. Instead of expressing the compositions of the excited state wave functions in terms of linear combination coefficients in the configuration expansions, we analyzed the NTOs to describe the nature of the electronic transitions with a condensed single pair of orbitals. The results of TD-DFT calculations are summarized in Tables S29-S31. From these analyses, the natures of the two newly emerged broad bands in the visible spectral domain for the MVS monocations were characterized: the lowest energy bands are $\mathbf{D_1}$-to-$\mathbf{D_2}$ transitions and the second lowest energy bands are naphthalene(s) nearby $\mathbf{D_2}$-to-$\mathbf{D_2}$ transitions. These TD-DFT results predict that all S_1 states of the three MVSs considered in this study possess strong IVCT character, allowing for analysis of spectroelectrochemical data in terms of the Mulliken-Hush IVCT relation.

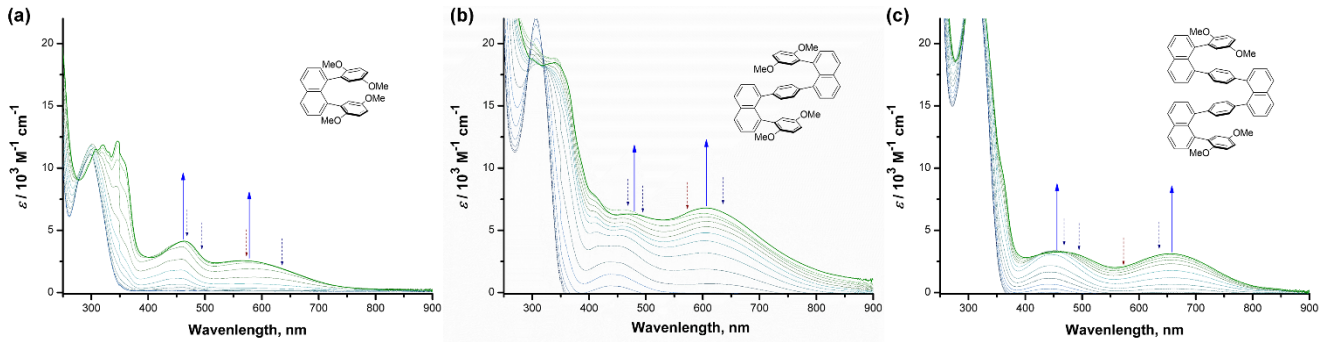

Figure 9. Spectroelectrochemical UV/vis/NIR absorption spectra recorded for **1** (a), **2** (b), and **3** (c) in an OTTLE cell. Terminal spectra correspond to those characteristic of the monocationic species. Blue arrows indicate the low energy spectral envelopes of the MV cation radicals. Blue and red dashed arrows indicate the positions of the cation radical absorption maxima of dimethoxybenzene and naphthalene, respectively.

See SI for the spectroelectrochemical absorption spectra of dimethoxybenzene and naphthalene. Experimental conditions: [compound] = 6 mM; [$TBAPF_6$] = 0.1 M; solvent = CH_2Cl_2:CH_3CN = 3:2; temperature = 25 ºC; pathlength = 2 μm.

In order to extract the absorption band associated with the lowest energy $S_0 \rightarrow S_1$ transition from the spectral envelope, we analyzed spectroeletrochemical data using multi-peak Gaussian deconvolution. Overlay plots of experimentally determined absorption spectra with deconvoluted Gaussian components are displayed in Figure 10.

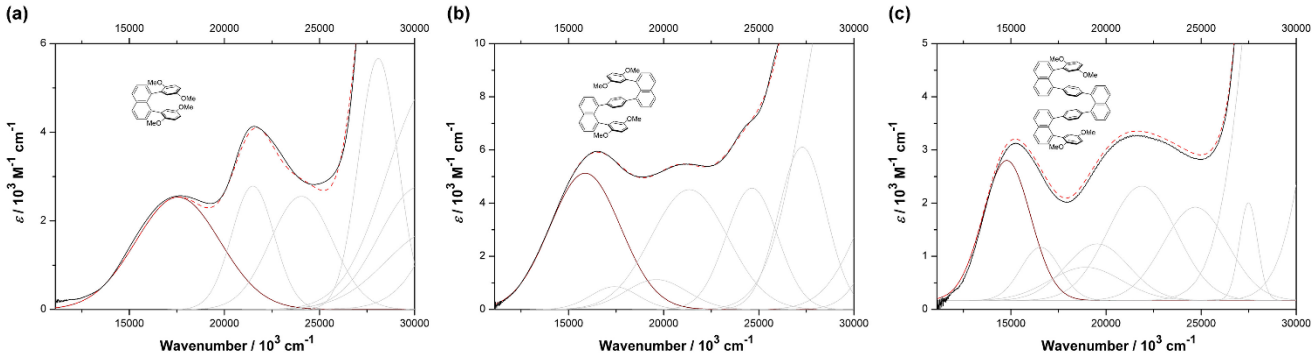

Figure 10. Overlay plots of experimentally determined absorption spectra of $\mathbf{1}^{\bullet+}$ (a), $\mathbf{2}^{\bullet+}$ (b), and $\mathbf{3}^{\bullet+}$ (c) (black solid lines) with multi-peak Gaussian deconvolutions (red and gray thin lines for individual components and red dashed line for their summation). The lowest energy component that corresponds to the $S_0 \rightarrow S_1$ transition is described by the red line.

Electronic Coupling

The presence of IVCT bands in the three MVS models enables us to evaluate electronic coupling directly from the experimental data. Fitting parameters obtained from the deconvoluted Gaussian peaks of the lowest energy bands are summarized in Table 5. Note that absorption band maxima are observed to shift toward the red as the distance (R) between $\mathbf{D_1}$ and $\mathbf{D_2}$ increases for these class II MVSs; these excitation energies correspond to the λ values for the $\mathbf{1}^{\bullet+}$, $\mathbf{2}^{\bullet+}$, and $\mathbf{3}^{\bullet+}$ systems. As the distance between

D₁ and **D₂** increases, the degree of charge-resonance (ζ) and geometry distortions both decrease, congruent with the dependence of the λ value magnitude on molecular size.

The H_{12} values of the three MVSs were calculated according to eq. 2 with fitting parameters of the lowest energy IVCT band denoted as $H_{12,exp}$. The largest $H_{12,exp}$ value was 2906 cm^{-1} for **1**$^{\bullet+}$, 1/6 of the λ value of **1**$^{\bullet+}$ and thus far below the class II-class III borderline where $H_{12} = \lambda/2$. Therefore, all MVSs in this work can be confirmed as class II systems. The distance dependence of $H_{12,exp}$ values was evaluated by plotting $\ln(H_{12,exp})^2$ vs R_{12}, which is displayed in Figure 11. A good linear correlation (R = 0.979) was observed and the decay parameter (β) was found to be 0.37.

Table 5. Fit parameters determined by the deconvolution of the spectroelectrochemical IVCT bands and Mulliken-Hush Analysis

MVS	R_{12}[a]	ε_{max}	ν_{max}[b]	ν_{FWHM}	$H_{12,exp}$[c]	$H_{12,DFT}$[d]	λ[e]	$\Delta G^{\ddagger}$	k_{ET}
	Å	$M^{-1}cm^{-1}$	cm^{-1}	cm^{-1}	cm^{-1}	cm^{-1}	eV	Kcal/mol	s^{-1}
1$^{\bullet+}$	3.29	2535	17556	5222	2906	3255	2.18	5.62	1.13×10^{11}
2$^{\bullet+}$	7.01	5126	15877	4375	1714	1604	1.97	6.98	4.13×10^{9}
3$^{\bullet+}$	10.14	3127	15151	3602	820	924	1.88	8.61	6.12×10^{7}

[a]**D₁** centroid-to-**D₂** centroid distances.[31] [b]ΔE [c]From IVCT analysis. [d]From Table 4. [e]Reorganization energy.

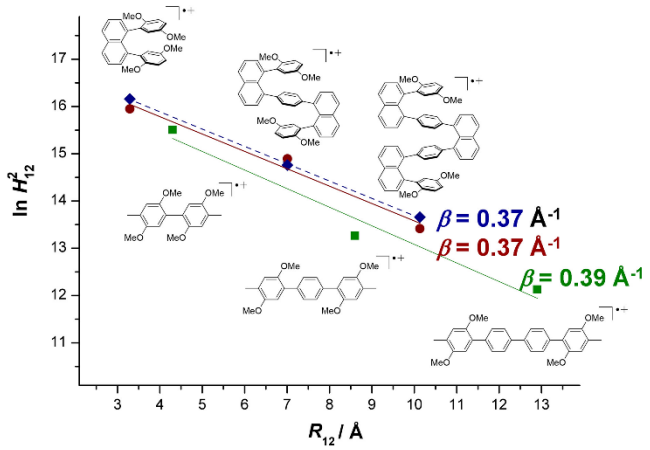

Figure 11. Distance dependence of the electronic coupling matrix element magnitudes determined by IVCT band analysis of the $\mathbf{1}^{\bullet+}$, $\mathbf{2}^{\bullet+}$, and $\mathbf{3}^{\bullet+}$ electronic absorption spectra ($H_{12,exp}$, red circle and red solid line), and the bond length analysis derived from the DFT calculational results ($H_{12,DFT}$, blue diamond and blue dashed line) for the . The results from ref.82 are co-plotted in green.

In an earlier section of this manuscript, we calculated the charge-resonance values (ζ) using geometric parameters obtained from DFT calculations (Table 4). These ζ values can be used to calculate H_{12} according to eq. 5, by adopting experimentally obtained ν_{max} values as ΔE. In Table 4, ζ values were evaluated for both $\mathbf{D_1}$ and $\mathbf{D_2}$ for 12 different diastereomers. The H_{12} values for $\mathbf{1}^{\bullet+}$, $\mathbf{2}^{\bullet+}$, and $\mathbf{3}^{\bullet+}$ were calculated by weighting relative occupancies of *syn* and *anti* orientations, and then averaging over $\mathbf{D_1}$ and $\mathbf{D_2}$. The obtained values were denoted as $H_{12,DFT}$ and are listed adjacent to $H_{12,exp}$ values in Table 5. Plotting $\ln(H_{12,DFT})^2$ vs R_{12} gave $\beta = 0.37$ Å^{-1}, with a near perfect linear correlation ($R = 0.999$).

The electronic coupling matrix element magnitues, as well as the decay parameters evaluated from experimental data and computational studies, were surprisingly similar to each other, as shown in Figure 11. It is worth noting that the distance dependence of electronic coupling for photoinduced CS and thermal CR determined for a related π-stacked porphyrin donor (**P**)-aromatic spacer-quinone acceptor (**Q**) series that utilized an indentical 1,8-naphthyl pillaring motif were respectively determined to be 0.62 and 0.63 Å^{-1},[21] which are nearly a factor of 2 larger than those obtained in this work. In this regard, the H_{12} value of **3a-Zn** in which the porphyrin donor and quinone acceptor were separated by two π-stacked phenylene spacers[21] and the distance between **P** and **Q** was estimated to be 10.6 Å, similar to that between $\mathbf{D_1}$ and $\mathbf{D_2}$ of $\mathbf{3}^{\bullet+}$, was only 17 cm^{-1}, while the magnitude of $H_{12,exp}$ for $\mathbf{3}^{\bullet+}$ was determined to be 820 cm^{-1}. The large differences between both the H_{12} value magnitudes and the distance dependence of the electronic coupling between these systems, which possess the exactly same π-stacked charge transporting media, is remarkable. There is a long-standing discussion in the literature regarding the distance dependences and bridge-mediated D-A couplings determined from intervalence spectra releative to those evaluated from photoinduced ET rate kinetics. Since the effective tunneling barriers are different for the two processes,

the couplings and decay constantant need not be the same.[106-107] Indeed, determining the couplings and their distance dependences using both charge transfer spectra and photoinduced ET kinetic measurements can help to determine the specific tunneling eneriges at play for bridge-mediated superexchange, thus providing a crucial link between theory and experiment.

It is interesting to compare these results to those reported by Kochi,[82-83,105] which evaluated electronic coupling in $\mathbf{D_m(ph)_nD_m^{\bullet+}}$ ($\mathbf{D_m}$ = 4-methyl-2,5-dimethoxybenzene and **(ph)** = 1,4-phenylene, n = 0, 1, 2) MVSs. These two MVSs have similar redox centers yet drastically different charge tunneling media: π-stacked vs laterally conjugated aromatic units. The H_{12} values of the $\mathbf{D_m(ph)_nD_m^{\bullet+}}$ MVS were evaluated via analysis of IVCT bands. The H_{12} value of the $\mathbf{D_m\text{-}D_m^{\bullet+}}$ systems was determined to be $\upsilon_{max}/2$, as it is a class III MVS. Those of $\mathbf{D_m(ph)D_m^{\bullet+}}$ and $\mathbf{D_m(ph)_2D_m^{\bullet+}}$ were determined using a Mulliken-Hush analysis of IVCT bands. The reported H_{12} values and associated separation distances were 2330, 760, and 430 cm^{-1} and 4.3, 8.6, and 12.9 Å for $\mathbf{D_m\text{-}D_m^{\bullet+}}$, $\mathbf{D_m(ph)D_m^{\bullet+}}$, and $\mathbf{D_m(ph)_2D_m^{\bullet+}}$, respectively. The resulting decay parameter was determined to be 0.39 $Å^{-1}$. These results are co-plotted in Figure 11. Both the H_{12} values and the decay parameters obtained from two different MVSs are similar, indicating that electronic coupling mediated by non-bonded π-stacked arenes can rival the through-bond mediated donor-acceptor electronic coupling provided by 1,4-oligophenylene spacer motifs.

With λ and $H_{12,exp.}$ values, the activation barriers of the ET reactions ($\Delta G^{\ddagger}$, Figure 1) were calculated using the following equation.[82]

$$\Delta G^{\ddagger} = (\lambda - 2H_{12})^2/4\lambda \qquad \text{(eq. 7)}$$

The $\Delta G^{\ddagger}$ values for $\mathbf{1^{\bullet+}}$, $\mathbf{2^{\bullet+}}$, and $\mathbf{3^{\bullet+}}$ were determined to be 5.62, 6.98, and 8.61 kcal/mol, respectively. As shown in Figure 1, the value of $\Delta G^{\ddagger}$ decreases as H_{12} increases, and eventually disappears when the MVS enters the class III regime. A gradual decrease of $\Delta G^{\ddagger}$ value magnitudes with decreasing $R_{12,}$ is a reflection of this trend. Moreover, the 5.62 kcal/mol $\Delta G^{\ddagger}$ value for $\mathbf{1^{+}}$, which reflects a sub-van der Waals separation distance of two **D** units (3.24 Å), clearly indicates that this species belongs to class II MVSs, contrary to $\mathbf{D_m\text{-}D_m^{\bullet+}}$, which is a class III MVS with an even longer $\mathbf{D_m\text{-}D_m}$ separation distance (4.30 Å).

$$k_{ET} = \frac{2\pi}{\hbar} \frac{H_{DA}^2}{\sqrt{4\pi\lambda_T k_B T}} exp\left(-\frac{\Delta G^{\ddagger}}{k_B T}\right) \qquad \text{(eq. 8)}$$

The ET rate constants (k_{ET}) for the three MVSs were estimated using eq. 8 to be approximately 8.9 ps, 242 ps, and 1.6 ns for **1**$^{\bullet+}$, **2**$^{\bullet+}$, and **3**$^{\bullet+}$, respectively. Despite the large H_{12} values, a sharp decrease in the ET rate constant magnitudes with distance is expected due to the intrinsic absence of a driving force in these systems.

Conclusion

The electronic coupling matrix elements of two locally charged diabatic states, D$^+$-D and D-D$^+$, were evaluated for 1,8-bis(2',5'-dimethoxybenzene-1'-yl)naphthalene (**1**), 1,4-bis(8'-(2",5"-dimethoxybenzene-1"-yl)naphthalen-1'-yl)benzene (**2**), or 1,8-bis(4'-(8"-(2"',5"'-dimethoxybenzene-1"'-yl)naphthalen-1"-yl)benzene-1'-yl)naphthalene (**3**) D-D sytems. The IVCT bands for **1**$^{\bullet+}$, **2**$^{\bullet+}$, and **3**$^{\bullet+}$ mixed-valence systems, generated by selective 1e oxidation using a spectroelectrochemical method, were evaluated using a Mulliken-Hush analysis. X-ray crystallographic data revealed that compounds **1**-**3** have a rigid, cofacial donor-(aromatic spacer)-donor alignment in which the π-stacked aromatic units are constrained at sub-van-der Waals contact distances. These structures were successfully reproduced by DFT calculations by employing a range-separated hybrid functional approach with Grimme's dispersion correction (LC-wPBE-D3) and a def2-TZVP basis set. The three-dimensional structures of the **1**$^{\bullet+}$, **2**$^{\bullet+}$, and **3**$^{\bullet+}$ mixed-valence systems obtained from these calculations, determined respective dimethoxybenezene-dimethoxybenezene centroid-to-centroid distances of 3.29, 7.01, and 10.14 Å. Although the ΔE value that separates the first and second oxidation potentials of compound **1** indicated that a Robin-Day classification of **1**$^{\bullet+}$ is ambiguous (0.3 V), the broken symmetry of the two dimethoxybenzene redox centers determined from the DFT calculations suggests that **1**$^+$ is best characterized as a class II MVS. A Mulliken-Hush analysis of the lowest energy IVCT bands, which were extracted from Gaussian deconvolution of the **1**$^{\bullet+}$, **2**$^{\bullet+}$, and **3**$^{\bullet+}$ electronic spectra, indicated that all these species were class II MVSs; this analysis determined: (i) respective reorganization energies of 2.18, 1.97,

and 1.88 eV for $\mathbf{1}^{\bullet+}$, $\mathbf{2}^{\bullet+}$, and $\mathbf{3}^{\bullet+}$, showing a gradual decrease in these values with increasing molecular size, and (ii) corresponding respective ET reaction barrier ($\Delta G^{\ddagger}$) values of 5.62, 6.98, and 8.61 kcal/mol, reflecting a decrease in electronic coupling with increasing distance, and (iii) respective electronic coupling matrix elements of 2906, 1714, and 820 cm^{-1} for $\mathbf{1}^{\bullet+}$, $\mathbf{2}^{\bullet+}$, and $\mathbf{3}^{\bullet+}$. The magnitudes of these electronic coupling matrix elements were consistent with those evaluated independently from the charge resonance contribution determined from the DFT calculated structures, which were respectively 3255, 1604, and 924 cm^{-1} for $\mathbf{1}^{\bullet+}$, $\mathbf{2}^{\bullet+}$, and $\mathbf{3}^{\bullet+}$. The decay parameters determined from experimental and computational data for the distance dependence of the electronic coupling (β = 0.37 $Å^{-1}$) were identical. The distance dependence of the electronic coupling for these π-stacked mixed valence systems is thus extraordinarily mild, and shallower than that determined for related MVSs featuring similar redox centers and *p*-phenylene spacers. These results suggest that longitudinal charge tunneling in non-bonded π-stacked conjugated organic structures can be even more efficient than transverse and through-bond mediated charge tunneling in 1,4-phenylene spacers, when π-cofacial aromatic residues are properly aligned.

ASSOCIATED CONTENT

Supporting Information

Synthetic details, characterization data, X-ray crystallographic data, computational data, Cartesian coordinates for all diastereomers, bond distance analysis of neutral and dicationic species, spectroelectrochemical data. This material is available free of charge via the Internet at http://pubs.acs.org.

AUTHOR INFORMATION

Corresponding Author

Michael J. Therien: michael.therien@duke.edu

Youn K. Kang: younkang@smu.ac.kr

ORCID

Michael J. Therien: 0000-0003-4876-0036

Youn K. Kang: 0000-0002-0415-1311

Notes

The authors declare no competing financial interests.

ACKNOWLEDGMENT This work was supported by the National Research Foundation of Korea (NRF) grant funded by the Korea Government (2015R1D1A1A01058566 and 2018R1D1A1B07049976) and the U.S. Department of Energy through Grant DE-SC0001517. This work was also supported by the Korea Institute of Science and Technology Information with supercomputing resources including technical support (KSC-2017-C2-0040 and KSC-2018-CHA-0068). The authors would like to thank Prof. David N. Beratan for his valuable discussions and comments.

Supporting Information Available: Synthesis and characterization data; NMR spectra; X-ray crystallographic data; theoretical computations. This material is available free of charge via the Internet at http://pubs.acs.org.

References

1. Coropceanu, V.; Cornil, J.; da Silva Filho, D. A.; Olivier, Y.; Silbey, R.; Brédas, J. L., Charge transport in organic semiconductors. *Chem. Rev.* **2007,** *107*, 926-952.
2. Shirota, Y.; Kageyama, H., Charge carrier transporting molecular materials and their applications in devices. *Chem. Rev.* **2007,** *107*, 953-1010.
3. Zaumseil, J.; Sirringhaus, H., Electron and ambipolar transport in organic field-effect transistors. *Chem. Rev.* **2007,** *107*, 1296-1323.
4. Arias, A. C.; MacKenzie, J. D.; McCulloch, I.; Rivnay, J.; Salleo, A., Materials and applications for large area electronics: Solution-based approaches. *Chem. Rev.* **2010,** *110*, 3-24.
5. Facchetti, A., π-Conjugated polymers for organic electronics and photovoltaic cell applications. *Chem. Mater.* **2011,** *23*, 733-758.

6. Dong, H.; Fu, X.; Liu, J.; Wang, Z.; Hu, W., 25th Anniversary Article: Key Points for High-Mobility Organic Field-Effect Transistors. *Adv.Mater*. **2013,** *25*, 6158-6183.
7. Guo, X.; Baumgarten, M.; Müllen, K., Designing π-conjugated polymers for organic electronics. *Prog. Polym. Sci*. **2013,** *38*, 1832-1908.
8. Miró, P.; Audiffred, M.; Heine, T., An atlas of two-dimensional materials. *Chem. Soc. Rev*. **2014,** *43*, 6537-6554.
9. Ostroverkhova, O., Organic Optoelectronic Materials: Mechanisms and Applications. *Chem. Rev*. **2016,** *116* , 13279-13412.
10. Atxabal, A.; Arnold, T.; Parui, S.; Hutsch, S.; Zuccatti, E.; Llopis, R.; Cinchetti, M.; Casanova, F.; Ortmann, F.; Hueso, L. E., Tuning the charge flow between Marcus regimes in an organic thin-film device. *Nat. Commun*. **2019,** *10*, 2089.
11. Stadtmüller, B.; Emmerich, S.; Jungkenn, D.; Haag, N.; Rollinger, M.; Eich, S.; Maniraj, M.; Aeschlimann, M.; Cinchetti, M.; Mathias, S., Strong modification of the transport level alignment in organic materials after optical excitation. *Nat. Commun*. **2019,** *10*, 1470.
12. Yokota, T.; Zalar, P.; Kaltenbrunner, M.; Jinno, H.; Matsuhisa, N.; Kitanosako, H.; Tachibana, Y.; Yukita, W.; Koizumi, M.; Someya, T., Ultraflexible organic photonic skin. *Sci. Adv*. **2016,** *2*, e1501856.
13. Oh, J. Y.; Rondeau-Gagné, S.; Chiu, Y. C.; Chortos, A.; Lissel, F.; Wang, G. J. N.; Schroeder, B. C.; Kurosawa, T.; Lopez, J.; Katsumata, T.; Xu, J.; Zhu, C.; Gu, X.; Bae, W. G.; Kim, Y.; Jin, L.; Chung, J. W.; Tok, J. B. H.; Bao, Z., Intrinsically stretchable and healable semiconducting polymer for organic transistors. *Nature*. **2016,** *539* , 411-415.
14. Rawson, J.; Angiolillo, P. J.; Therien, M. J., Extreme electron polaron spatial delocalization in ϕ-conjugated materials. *Proc. Natl. Acad. Sci. U. S. A*. **2015,** *112* , 13779-13783.
15. Kesters, J.; Verstappen, P.; Kelchtermans, M.; Lutsen, L.; Vanderzande, D.; Maes, W., Porphyrin-Based Bulk Heterojunction Organic Photovoltaics: The Rise of the Colors of Life. *Adv. Energy. Mater*. **2015,** *5*, 1500218..
16. Creutz, C.; Newton, M. D.; Sutin, N., Metal-Ligand and Metal-Metal Coupling Elements. *J. Photoch. Photobio. A*. **1994,** *82*, 47-59.
17. Beratan, D. N.; Betts, J. N.; Onuchic, J. N., Protein electron transfer rates set by the bridging secondary and tertiary structure. *Science*. **1991,** *252*, 1285-1288.
18. Risser, S. M.; Beratan, D. N.; Meade, T. J., Electron Transfer in DNA: Predictions of Exponential Growth and Decay of Coupling with Donor-Acceptor Distance. *J. Am. Chem. Soc*. **1993,** *115*, 2508-2510.
19. Barbara, P. F.; Meyer, T. J.; Ratner, M. A., Contemporary issues in electron transfer research. *J. Phys. Chem*. **1996,** *100*, 13148-13168.
20. Gray, H. B.; Winkler, J. R., Long-range electron transfer. *Proc. Natl. Acad. Sci. U. S. A*. **2005,** *102*, 3534-3539.
21. Kang, Y. K.; Iovine, P. M.; Therien, M. J., Electron transfer reactions of rigid, cofacially compressed, π-stacked porphyrin-bridge-quinone systems. *Coordin. Chem. Rev*. **2011,** *255*, 804-824 and references therein.
22. Brun, A. M.; Harriman, A., Dynamics of Electron-Transfer between Intercalated Polycyclic Molecules - Effect of Interspersed Bases. *J. Am. Chem. Soc*. **1992,** *114*, 3656-3660.
23. Murphy, C. J.; Arkin, M. R.; Jenkins, Y.; Ghatlia, N. D.; Bossmann, S. H.; Turro, N. J.; Barton, J. K., Long-range photoinduced electron transfer through a DNA helix. *Science*. **1993,** *262*, 1025-1029.
24. Arkin, M. R.; Stemp, E. D. A.; Holmlin, R. E.; Barton, J. K.; Hörmann, A.; Olson, E. J. C.; Barbara, P. F., Rates of DNA-mediated electron transfer between metallointercalators. *Science*. **1996,** *273*, 475-480.
25. Lewis, F. D.; Liu, X. Y.; Liu, J. Q.; Miller, S. E.; Hayes, R. T.; Wasielewski, M. R., Direct measurement of hole transport dynamics in DNA. *Nature*. **2000,** *406*, 51-53.

26. Lewis, F. D.; Wu, T. F.; Zhang, Y. F.; Letsinger, R. L.; Greenfield, S. R.; Wasielewski, M. R., Distance-dependent electron transfer in DNA hairpins. *Science*. **1997,** *277*, 673-676.
27. Meade, T. J.; Kayyem, J. F., Electron transfer through DNA: site-specific modification of duplex DNA with ruthenium donors and acceptors. *Angew. Chem. Int. Edit.* **1995,** *34*, 352-354.
28. Meggers, E.; Michel-Beyerle, M. E.; Giese, B., Sequence dependent long range hole transport in DNA. *J. Am. Chem. Soc.* **1998,** *120*, 12950-12955.
29. Fukui, K.; Tanaka, K., Distance dependence of photoinduced electron transfer in DNA. *Angew. Chem. Int. Edit.* **1998,** *37*, 158-161.
30. Kang, Y. K.; Rubtsov, I. V.; Iovine, P. M.; Chen, J. X.; Therien, M. J., Distance dependence of electron transfer in rigid, cofacially compressed, π-stacked porphyrin-bridge-quinone systems. *J. Am. Chem. Soc.* **2002,** *124*, 8275-8279.
31. Zheng, J.; Kang, Y. K.; Therien, M. J.; Beratan, D. N., Generalized Mulliken-Hush analysis of electronic coupling interactions in compressed π-stacked porphyrin-bridge-quinone systems. *J. Am. Chem. Soc.* **2005,** *127*, 11303-11310.
32. Wartini, A. R.; Staab, H. A.; Neugebauer, F. A., Intramolecular electron transfer between terminal 1,4-dimethoxybenzene units in radical cations with a [2.2](1,4)naphthalenophane, [2.2](1,4)anthracenophane, and pentacene skeleton. *Eur. J. Org. Chem.* **1998,** 1161-1170.
33. Wartini, A. R.; Valenzuela, J.; Staab, H. A.; Neugebauer, F. A., Intramolecular electron transfer between 2,5-dimethoxy-1,4-phenylene units in [n.n]paracyclophane radical cations. *Eur. J. Org. Chem.* **1998,** 139-148.
34. Wartini, A. R.; Valenzuela, J.; Staab, H. A.; Neugebauer, F. A., [2.2]Paracyclophane-4,7,12,15-tetrone, [2.2](1,4)naphthalenophane-4,7,14,17-tetrone, and 1,4,8,11-pentacenetetrone radical anions - A comparative ESR study. *Eur. J. Org. Chem.* **1998,** 221-227.
35. Amthor, S.; Lambert, C., [2.2]Paracyclophane-bridged mixed-valence compounds: Application of a generalized mulliken-hush three-level model. *J. Phys. Chem. A* **2006,** *110*, 1177-1189.
36. Kattnig, D. R.; Mladenova, B.; Grampp, G.; Kaiser, C.; Heckmann, A.; Lambert, C., Electron paramagnetic resonance spectroscopy of bis(triarylamine) paracyclophanes as model compounds for the intermolecular charge-transfer in solid state materials for optoelectronic applications. *J. Phys. Chem. C* **2009,** *113*, 2983-2995.
37. Vura-Weis, J.; Abdelwahed, S. H.; Shukla, R.; Rathore, R.; Ratner, M. A.; Wasielewski, M. R., Crossover from Single-Step Tunneling to Multistep Hopping for Molecular Triplet Energy Transfer. *Science*. **2010,** *328*, 1547.
38. Navale, T. S.; Thakur, K.; Vyas, V. S.; Wadumethrige, S. H.; Shukla, R.; Lindeman, S. V.; Rathore, R., Charge delocalization in self-assembled mixed-valence aromatic cation radicals. *Langmuir*. **2012,** *28*, 71-83.
39. Wang, D.; Talipov, M. R.; Ivanov, M. V.; Rathore, R., Energy Gap between the Poly-p-phenylene Bridge and Donor Groups Controls the Hole Delocalization in Donor-Bridge-Donor Wires. *J. Am. Chem. Soc.* **2016,** *138*, 16337-16344.
40. Robin, M. B.; Day, P., Mixed Valence Chemistry-A Survey and Classification. In *Adv. Inorg. Chem.* **1968,** *10*, 247-422.
41. Tom, G. M.; Creutz, C.; Taube, H., Mixed Valence Complexes of Ruthenium Ammines with 4,4′-Bipyridine as Bridging Ligand. *J. Am. Chem. Soc.* **1974,** *96*, 7827-7829.
42. Creutz, C., Mixed-Valence Complexes of d^5-d^6 Metal Centers. *Prog. Inorg. Chem.* **1983,** *30*, 1-73.
43. Richardson, D. E.; Taube, H., Mixed-Valence Molecules - Electronic Delocalization and Stabilization. *Coord.. Chem. Rev.* **1984,** *60*, 107-129.
44. Kaim, W.; Klein, A.; Glockle, M., Exploration of mixed-valence chemistry: Inventing new analogues of the Creutz-Taube ion. *Accounts. Chem. Res.* **2000,** *33*, 755-763.
45. Launay, J. P., Long-distance intervalence electron transfer. *Chem. Soc. Rev.* **2001,** *30*, 386-397.
46. D'Alessandro, D. M.; Keene, F. R., Current trends and future challenges in the experimental, theoretical and computational analysis of intervalence charge transfer (IVCT) transitions. *Chem. Soc. Rev.* **2006,** *35*, 424-440.

47. Creutz, C., Mixed Valence Complexes of d^5-d^6 Metal Centers. *Prog. Inorg. Chem.*, **2007** *30*, 1-73.
48. Hankache, J.; Wenger, O. S., Organic mixed valence. *Chem. Rev.* **2011,** *111*, 5138-5178.
49. Heckmann, A.; Lambert, C., Organic mixed-valence compounds: A playground for electrons and holes. *Angew. Chem. Int. Edit.* **2012,** *51*, 326-392.
50. Parthey, M.; Kaupp, M., Quantum-chemical insights into mixed-valence systems: Within and beyond the Robin-Day scheme. *Chem. Soc. Rev.* **2014,** *43*, 5067-5088.
51. Morrison, W. H.; Hendrickson, D. N., Electron Transfer in Oxidized Biferrocene, Biferrocenylene, and [1.1]Ferrocenophane Systems. *Inorg. Chem.* **1975,** *14*, 2331-2346.
52. Torrance, J. B.; Scott, B. A.; Welber, B.; Kaufman, F. B.; Seiden, P. E., Optical properties of the radical cation tetrathiafulvalenium (TTF^+) in its mixed-valence and monovalence halide salts. *Phys. Rev. B* **1979,** *19*, 730-741.
53. Coleman, P., New approach to the mixed-valence problem. *Phys. Rev. B* **1984,** *29*, 3035-3044.
54. Coropceanu, V.; Malagoli, M.; André, J. M.; Brédas, J. L., Intervalence transition in triarylamine mixed-valence systems: A time-dependent density functional theory study. *J. Chem. Phys.* **2001,** *115*, 10409-10416.
55. Nelsen, S. F.; Konradsson, A. E.; Telo, J. P., Pseudo-para-dinitro[2.2]paracyclophane radical anion, a mixed-valence system poised on the class II/class III borderline. *J. Am. Chem. Soc.* **2005,** *127*, 920-925.
56. Kaupp, M.; Renz, M.; Parthey, M.; Stolte, M.; Würthner, F.; Lambert, C., Computational and spectroscopic studies of organic mixed-valence compounds: Where is the charge? *Phys. Chem. Chem. Phys.* **2011,** *13*, 16973-16986.
57. Diallo, A. K.; Absalon, C.; Ruiz, J.; Astruc, D., Ferrocenyl-terminated redox stars: Synthesis and electrostatic effects in mixed-valence stabilization. *J. Am. Chem. Soc.* **2011,** *133*, 629-641.
58. Brunschwig, B. S.; Creutz, C.; Sutin, N., Optical transitions of symmetrical mixed-valence systems in the Class II-III transition regime. *Chem. Soc. Rev.* **2002,** *31*, 168-184.
59. Demadis, K. D.; Hartshorn, C. M.; Meyer, T. J., The localized-to-delocalized transition in mixed-valence chemistry. *Chem. Rev.* **2001,** *101*, 2655-2685.
60. Sauvage, J. P.; Collin, J. P.; Chambron, J. C.; Guillerez, S.; Coudret, C.; Balzani, V.; Barigelletti, F.; Decola, L.; Flamigni, L., Ruthenium(Ii) and Osmium(Ii) Bis(Terpyridine) Complexes in Covalently-Linked Multicomponent Systems - Synthesis, Electrochemical-Behavior, Absorption-Spectra, and Photochemical and Photophysical Properties. *Chem. Rev.* **1994,** *94*, 993-1019.
61. Newton, M. D., Quantum Chemical Probes of Electron-Transfer Kinetics - the Nature of Donor-Acceptor Interactions. *Chem. Rev.* **1991,** *91*, 767-792.
62. Sun, D.; Rosokha, S. V.; Kochi, J. K., Donor-acceptor (electronic) coupling in the precursor complex to organic electron transfer: Intermolecular and intramolecular self-exchange between phenothiazine redox centers. *J. Am. Chem. Soc.* **2004,** *126*, 1388-1401.
63. Bailey, S. E.; Zink, J. I.; Nelsen, S. F., Contributions of symmetric and asymmetric normal coordinates to the intervalence electronic absorption and resonance Raman spectra of a strongly coupled p-phenylenediamine radical cation. *J. Am. Chem. Soc.* **2003,** *125*, 5939-5947.
64. Cooley, L. F.; Han, H.; Zimmt, M. B., Evaluation of electronic coupling in a donor-bridge-acceptor molecule: A fluorescence polarization anisotropy investigation. *J. Phys. Chem. A* **2002,** *106*, 884-892.
65. Bixon, M.; Jortner, J.; Verhoeven, J. W., Lifetimes for Radiative Charge Recombination in Donor-Acceptor Molecules. *J. Am. Chem. Soc.* **1994,** *116*, 7349-7355.
66. Gould, I. R.; Young, R. H.; Mueller, L. J.; Albrecht, A. C.; Farid, S., Electronic Coupling Matrix-Elements in Acceptor-Donor Excited-States and the Effect of Charge-Transfer Character on Their Radiative Rate Constants. *J. Am. Chem. Soc.* **1994,** *116*, 3147-3148.
67. Reimers, J. R.; Hush, N. S., Electron transfer and energy transfer through bridged systems. 4. Intermetallic couplin and electronic spectra of the bis(pentaammineruthenium) complexes of α,ω-dipyridyl *trans*-polyenes in D_2O. *Inorg. Chem.* **1990,** *29*, 3686-3697.

68. Oevering, H.; Verhoeven, J. W.; Paddonrow, M. N.; Warman, J. M., Charge-Transfer Absorption and Emission Resulting from Long-Range through-Bond Interaction - Exploring the Relation between Electronic Coupling and Electron-Transfer in Bridged Donor-Acceptor Systems. *Tetrahedron*. **1989,** *45*, 4751-4766.
69. Desbois, M. H.; Astruc, D.; Guillin, J.; Mariot, J. P.; Varret, F., Organometallic Electron Reservoirs .23. 36-Electron to 40-Electron Complexes $(C_6R_6FeCp\text{-}CpFe\ C_6R_6)^{n\pm}$ (R = H, Me; n = 0-2) and the 1st Delocalized Mixed-Valence Complexes Containing Fe^{I}. *J. Am. Chem. Soc*. **1985,** *107*, 5280-5282.
70. Mulliken, R. S., Molecular Compounds and Their Spectra .2. *J. Am. Chem. Soc*. **1952,** *74*, 811-824.
71. Hush, N. S., Intervalence-transfer absorption. Part 2. Theoretical considerations and spectroscopic data *Prog. Inorg. Chem*. **1967,** *8*, 391-444.
72. Hush, N. S., Homogeneous and Heterogeneous Optical and Thermal Electron Transfer. *Electrochim. Acta*. **1968,** *13*, 1005-1023.
73. Sutin, N., Theory of Electron-Transfer Reactions - Insights and Hindsights. *Prog. Inorg. Chem*. **1983,** *30*, 441-498.
74. Cave, R. J.; Newton, M. D., Generalization of the Mulliken-Hush treatment for the calculation of electron transfer matrix elements. *Chem. Phys. Lett*. **1996,** *249*, 15-19.
75. Cave, R. J.; Newton, M. D., Calculation of electronic coupling matrix elements for ground and excited state electron transfer reactions: Comparison of the generalized Mulliken-Hush and block diagonalization methods. *J. Chem. Phys*. **1997,** *106*, 9213-9226.
76. Zheng, J. R.; Kang, Y. K.; Therien, M. J.; Beratan, D. N., Generalized Mulliken-Hush analysis of electronic coupling interactions in compressed π-stacked porphyrin-bridge-quinone systems. *J. Am. Chem. Soc*. **2005,** *127*, 11303-11310.
77. Voityuk, A. A., Donor-acceptor electronic couplings in π- stacks: How many states must be accounted for? *Chem. Phys. Lett*. **2006,** *422*, 15-19.
78. In this two state model, the overlap integral *S* is neglected.
79. Rubtsov, I. V.; Kang, Y. K.; Redmore, N. P.; Allen, R. M.; Zheng, J. R.; Beratan, D. N.; Therien, M. J., The degree of charge transfer in ground and charge-separated states revealed by ultrafast visible pump/mid-IR probe spectroscopy. *J. Am. Chem. Soc*. **2004,** *126*, 5022-5023.
80. Kim, H. M.; Park, J.; Lee, Y. T.; Lim, M.; Chung, Y. K.; Kang, Y. K., Probing ground-to-CT state electronic coupling for the system with no apparent charge transfer absorption intensity by ultrafast visible-pump/Mid-IR- probe spectroscopy. *J. Phys. Chem. C* **2011,** *115*, 22557-22562.
81. Caspar, J. V.; Westmoreland, T. D.; Allen, G. H.; Bradley, P. G.; Meyer, T. J.; Woodruff, W. H., Molecular and Electronic-Structure in the Metal-to-Ligand Charge-Transfer Excited-States of d^6 Transition-Metal Complexes in Solution. *J. Am. Chem. Soc*. **1984,** *106*, 3492-3500.
82. Lindeman, S. V.; Rosokha, S. V.; Sun, D.; Kochi, J. K., X-ray structure analysis and the intervalent electron transfer in organic mixed-valence crystals with bridged aromatic cation radicals. *J. Am. Chem. Soc*. **2002,** *124*, 843-855.
83. Sun, D. L.; Rosokha, S. V.; Lindeman, S. V.; Kochi, J. K., Intervalence (Charge-Resonance) Transitions in Organic Mixed-Valence Systems. Through-Space versus Through-Bond Electron Transfer between Bridged Aromatic (Redox) Centers. *J. Am. Chem. Soc*. **2003,** *125*, 15950-15963.
84. Kang, Y. K.; Duncan, T. V.; Therien, M. J., Temperature-dependent mechanistic transition for photoinduced electron transfer modulated by excited-state vibrational relaxation dynamics. *J. Phys. Chem. B* **2007,** *111*, 6829-6838.
85. Krejčik, M.; Daněk, M.; Hartl, F., Simple construction of an infrared optically transparent thin-layer electrochemical cell. Applications to the redox reactions of ferrocene, $Mn_2(CO)_{10}$ and $Mn(CO)_3$ (3,5-di-*t*-butyl-catecholate). *J. Electroanal. Chem*. **1991,** *317*, 179-187.
86. Sheldrick, G. M., A short history of SHELX. *Acta. Crystallogr. A* **2008,** *64*, 112-122.
87. Sheldrick, G. M., Crystal structure refinement with SHELXL. *Acta Crystallogr. C* **2015,** *71*, 3-8.
88. Frisch, M. J. e. a., *Gaussian 16, Revision A.03; Gaussian, Inc.: Wallingford, CT,* **2016**.

89. Moellmann, J.; Grimme, S., DFT-D3 study of some molecular crystals. *J. Phys. Chem. C* **2014,** *118*, 7615-7621.
90. Grimme, S., Semiempirical GGA-type density functional constructed with a long-range dispersion correction. *J. Comput. Chem.* **2006,** *27*, 1787-1799.
91. Grimme, S., Semiempirical hybrid density functional with perturbative second-order correlation. *J. Chem. Phys.* **2006,** *124*, 034108.
92. Grimme, S.; Antony, J.; Ehrlich, S.; Krieg, H., A consistent and accurate ab initio parametrization of density functional dispersion correction (DFT-D) for the 94 elements H-Pu. *J. Chem. Phys.* **2010,** *132*, 154104.
93. Grimme, S.; Ehrlich, S.; Goerigk, L., Effect of the damping function in dispersion corrected density functional theory. *J. Comput. Chem.* **2011,** *32*, 1456-1465.
94. Miertuš, S.; Scrocco, E.; Tomasi, J., Electrostatic interaction of a solute with a continuum. A direct utilizaion of AB initio molecular potentials for the prevision of solvent effects. *Chem. Phys.* **1981,** *55*, 117-129.
95. Miertus˜, S.; Tomasi, J., Approximate evaluations of the electrostatic free energy and internal energy changes in solution processes. *Chem. Phys.* **1982,** *65*, 239-245.
96. Tomasi, J.; Mennucci, B.; Cammi, R., Quantum mechanical continuum solvation models. *Chem. Rev.* **2005,** *105*, 2999-3093.
97. Barone, V.; Cossi, M., Quantum calculation of molecular energies and energy gradients in solution by a conductor solvent model. *J. Phys. Chem. A* **1998,** *102*, 1995-2001.
98. Cossi, M.; Rega, N.; Scalmani, G.; Barone, V., Energies, structures, and electronic properties of molecules in solution with the C-PCM solvation model. *J. Comput. Chem.* **2003,** *24*, 669-681.
99. Runge, E.; Gross, E. K. U., Density-Functional Theory for Time-Dependent Systems. *Phys. Rev. Lett.* **1984,** *52*, 997-1000.
100. Bartolotti, L. J., Time-Dependent Kohn-Sham Density-Functional Theory. *Phys. Rev. A* **1982,** *26*, 2243-2244.
101. Martin, R. L., Natural transition orbitals. *J. Chem. Phys.* **2003,** *118*, 4775-4777.
102. Iovine, P. M.; Kellett, M. A.; Redmore, N. P.; Therien, M. J., Syntheses and ^{1}H-NMR spectroscopy of rigid, cofacially aligned, porphyrin-bridge-quinone systems in which the interplanar separations between the porphyrin, aromatic bridge, and quinone are less than the sum of their respective van der Waals radii. *J. Am. Chem. Soc.* **2000,** *122*, 8717-8727.
103. Iovine, P. M.; Veglia, G.; Furst, G.; Therien, M. J., High-resolution structure and conformational dynamics of rigid, cofacially aligned porphyrin-bridge-quinone systems as determined by NMR spectroscopy and ab initio simulated annealing calculations. *J. Am. Chem. Soc.* **2001,** *123*, 5668-5679.
104. Renz, M.; Theilacker, K.; Lambert, C.; Kaupp, M., A reliable quantum-chemical protocol for the characterization of organic mixed-valence compounds. *J. Am. Chem. Soc.* **2009,** *131*, 16292-16302.
105. Sun, D.; Lindeman, S. V.; Rathore, R.; Kochi, J. K., Intramolecular (electron) delocalization between aromatic donors and their tethered cation-radicals. Application of electrochemical and structural probes. *J. Chem. Soc, Perkin Transactions 2* **2001,** 1585-1594.
106. Redi, M.; Hopfield, J. J., Theory of thermal and photoassisted electron tunneling. *The J. Chem. Phys.* **1979,** *72*, 6651-6660.
107. Beratan, D. N.; Hopfield, J. J., Calculation of Electron Tunneling Matrix Elements in Rigid Systems: Mixed-Valence Dithiaspirocyclobutane Molecules. *J. Am. Chem. Soc.* **1984,** *106*, 1584-1594

SYNOPSIS TOC